Uncovering the multi-step process of stable microtubule bundle formation upon entry into quiescence

Damien Laporte[1]*, Aurélie Massoni-Laporte[1], Charles Lefranc[1], Jim Dompierre[1], David Mauboules[1], Emmanuel. T. Nsamba[2], Anne Royou[1], Lihi Gal[3], Maya Schuldiner[3], Mohan L. Gupta Jr[2], Isabelle Sagot[1]

Affiliation :

1: Univ. Bordeaux, CNRS, IBGC, UMR 5095, Bordeaux, France

2: Genetics, Development, and Cell Biology, Iowa State University, Ames, IA 50011, USA.

3: Department of Molecular Genetics, Weizmann Institute of Science, Rehovot, Israel

* Corresponding author: Damien.laporte@ibgc.cnrs.fr

Abstract

Cells fine-tune microtubule assembly in both space and time, to give rise to distinct edifices with specific cellular functions. In proliferating cells, microtubules are highly dynamics, yet, proliferation cessation often lead to their stabilization. One of the most stable microtubule structures identified to date is the nuclear bundle assembled in yeast quiescent cells. In this report, we characterize the original multistep process driving the assembly of this structure. We show that its follows a precise temporality that relies on the sequential action of specific kinesin-14/kinesins-5 and involves both microtubule-kinetochore and kinetochore-kinetochore interactions. Upon quiescence exit, the microtubule bundle disassembles via a cooperative process involving the Kinesin-8 and its full disassembly is required to authorize cells re-entry into proliferation. Overall, our study not only provides the first description, at the molecular scale, of the entire life cycle of a stable microtubule structure *in vivo*, but also sheds light on its function as a sort of “checkpoint” for cell cycle resumption.

32 **Introduction**

33 Microtubules (MT) are hollow cylindrical polymers assembled by the non-covalent
34 interaction of α- and β-tubulin heterodimers. MTs are generally nucleated at MT organizing
35 centers (MTOC) by a ɣ-tubulin complex (ɣ-TuC) that acts as a template and stabilizes the so-
36 called MT "minus-end" (Liu et al., 2021; Roostalu and Surrey, 2017; Sanchez and Feldman,
37 2017; Thawani and Petry, 2021). At the opposite end, the "plus-end" (+end), MTs elongate
38 by the addition of GTP tubulin. The β-tubulin bound GTP is hydrolyzed and stable but
39 transient GDP + Pi intermediates are generated in the region immediately trailing the
40 growing +end. A subsequent Pi release favors MT depolymerization that can be rescued by
41 *de novo* GTP-tubulin addition (Cleary and Hancock, 2021; Gudimchuk and McIntosh, 2021).
42 As such, MTs alternate periods of growth and shrinkage, a behavior called dynamic
43 instability (Mitchison and Kirschner, 1984). *In vivo*, a profusion of MT associated proteins
44 (MAPs) regulate MT length and dynamics (Bodakuntla et al., 2019; Goodson and Jonasson,
45 2018). Besides, MTs are often assembled from multiple tubulin variants or isotypes, and
46 modified by a cohort of post-translational modifications that modulate MT dynamics directly
47 or by influencing the recruitment of MAPs (Janke and Magiera, 2020; Roll-Mecak, 2020).
48 Other MAPs organize MTs into high-ordered edifices either by cross-linking MTs or by
49 connecting them with cellular structures such as membranes, chromosomes or components
50 of the actin cytoskeleton (Bodakuntla et al., 2019; Meiring et al., 2020). Cells fine-tune these
51 mechanisms both in space and in time to give rise to distinct MT architectures with specific
52 function.

53 In proliferating cells, MT dynamic is crucial for their functions. It allows exploring the
54 cell volume searching for structures to "capture", like centromeres during mitosis, or to
55 exert pushing or pulling forces required for various cellular processes such as cell migration

56 or morphogenesis (Heald and Khodjakov, 2015; Kirschner and Mitchison, 1986). Yet, the MT
57 cytoskeleton can extensively rearrange and assemble more stable MT structures, notably
58 when cells change fate (Meiring et al., 2020; Röper, 2020). For example, in terminally-
59 differentiated cells, such as epithelial cells, cardiomyocytes or neurons, stable MT networks
60 make up the majority, and ensure critical cellular functions such as cell shape maintenance
61 or long-distance intra-cellular transport (Baas et al., 2016; Muroyama and Lechler, 2017).
62 Defects in MT stabilization are at the origin of many human pathologies, including neuro-
63 degenerative diseases and ciliopathies (Anvarian et al., 2019; Wheway et al., 2018). Effectors
64 responsible for MT stabilization have been actively searched for since the 1980's. In
65 mammals, the involvement of specific MAPs such as Tau, MAP2, MAP6 and PRC1, or tubulin
66 post-translational modifications have been extensively studied. While their contributions to
67 MT stabilization are central and undisputable, their sole actions do not fully explain the
68 observed levels of MT stability in many types of non-dividing cells (Hahn et al., 2019).
69 For years, yeast species have been instrumental in deciphering mechanisms that
70 regulate MT dynamics in eukaryotes. While proliferating yeast cells display a dynamic MT
71 network (Winey and Bloom, 2012), proliferation cessation goes with the formation of
72 dramatically stable MT structures in both *S. cerevisiae* and *S. pombe* (Laporte and Sagot,
73 2014; Laporte et al., 2013, 2015). Upon quiescence establishment, *S. cerevisiae* assemble a
74 bundle composed of stable parallel MTs, hereafter called Q-nMT bundle, for Quiescent-cell
75 nuclear Microtubule bundle, that emanates from the nuclear side of the spindle pole body
76 (SPB), the yeast equivalent of the centrosome. The Q-nMT bundle spans the entire nucleus
77 and relocalizes kinetochores and centromeres that remain attached to its MT +ends (Laporte
78 and Sagot, 2014). Since MTs embedded into the Q-nMT bundle are not all of the same
79 length, they confer to the structure a typical arrow shape. When cells exit quiescence, the Q-

80 nMT bundle depolymerizes and, by pulling the attached centromeres back to the SPB, allows
81 the recovery of the typical Rabl-like configuration of chromosomes found in G1 yeast cells
82 (Jin et al., 1998). The molecular mechanisms underlying the formation of this peculiar stable
83 MT structure and its physiological function(s) are not understood. Yet, cells impaired for Q-
84 nMT bundle formation have a compromised survival rate in quiescence and a drastically
85 reduced fitness upon cell cycle re-entry (Laporte and Sagot, 2014; Laporte et al., 2013,
86 2015).

87 Here, we demonstrate that the Q-nMT bundle formation is a multistep process that
88 follows a precise temporal sequence. The first step requires the kinesin-14 Kar3, its regulator
89 Cik1 and the EB1 homolog Bim1, and leads to the formation of a short (≈ 1 µm) and stable
90 bundle that resembles a half mitotic spindle. Importantly, in this first step, MT
91 polymerization and stabilization are coupled. In a second step, additional MTs polymerize
92 from the SPB, elongate, and are zipped to pre-existing ones in a Cin8/kinesin-5 dependant
93 manner. The full Q-nMT bundle stabilization is established in a third and last step that
94 requires the kinesin-5 Kip1. Our observations further indicate that Q-nMT bundle assembly
95 requires not only MT-kinetochore attachment but also inter-kinetochore interactions.
96 Finally, we show that, upon quiescence exit, the Q-nMT bundle disassembles from its +ends,
97 where each MT depolymerizes in coordination with its neighbors, via the action of the
98 depolymerase Kip3, a member of the kinesin-8 family. A complete Q-nMT bundle
99 disassembly is required to authorize cells re-entry into the proliferation cycle. Overall, this
100 study describes for the first time the entire life cycle of a MT structure from the molecular
101 mechanisms involved in its formation and stabilization to its disassembly and further reveals
102 that this atypical quiescent specific structure acts as a sort of “checkpoint” for cell cycle
103 resumption upon quiescence exit.

104 ## Results

105 **The Q-nMT bundle formation is a three-step process**

106 To investigate whether the Q-nMT bundle was stable by default, *i.e.* intrinsically
107 stable, or assembled as a dynamic structure and then stabilized, we quantified Q-nMT
108 bundle length (Fig. 1A) and thickness (Fig. 1B) upon quiescence establishment following
109 carbon source exhaustion. We found that the Q-nMT bundle assembly was a 3-step process.
110 In an initial phase (phase I), MTs elongated from the SPB to reach ≈0.8 µm. The number of
111 these so-called phase I-MTs was about the same as in a mitotic spindle (see inset of Fig. 1B
112 and Sup. Fig. 1A). Importantly, phase I-MTs are resistant to nocodazole (Noc), a MT poison
113 that causes dynamic MT depolymerization, indicating that their stabilization was
114 concomitant with their polymerization (Fig. 1A-B). In a second phase, that started ≈10h after
115 glucose exhaustion, additional MTs emerged from the SPB (phase II-MTs) and elongated
116 along phase-I MTs, approximatively doubling the thickness of the phase I MT bundle (Fig. 1B
117 and Sup Fig. 1A). At this stage, the tip of the newly elongated MTs were instable (Fig. 1A-B).
118 Full Q-nMT bundle stabilization was reached ≈48h after glucose exhaustion (phase III), as
119 Noc treatment affected neither Q-nMT bundle length nor its thickness (Fig. 1A-B and Sup.
120 Fig. 1B). Another way to shed light on the Q-nMT bundle formation steps was to plot Q-nMT
121 bundle width as a function of length for each individual cells before and after Noc treatment
122 (Fig. 1C).

123 To confirm the above multistep process, we first followed Nuf2-GFP, a protein that
124 localize at the MT +end. In phase I, Nuf2-GFP signal relocates from SPB to the distal part of
125 elongating Q-nMT bundles (Sup. Fig. 1D). In phase II, when cells were treated with Noc, the
126 Nuf2-GFP signal followed depolymerizing MTs (Fig. 1D), testifying for the instability of phase
127 II MTs. By contrast, the Nuf2-GFP signal remained immobile in phase III, when cells have fully

128 stabilized Q-nMT bundles (Fig. 1D). Second, we measured the γ-tubulin (Tub4) signal at the
129 SPB and found that Tub4 started accumulating at the SPB at the onset of phase I to reach a
130 plateau at the end of phase II (Fig. 1E and Sup. Fig. 1E). Interestingly, the amount of Tub4 at
131 the SPB was proportional to the thickness of the Q-nMT bundle (Sup. Fig. 1F). Finally, in
132 order to confirm the two waves of MT elongation, we developed a strain expressing mTQZ-
133 Tub1 from the endogenous TUB1 promoter and mRuby-TUB1 under the ADH2 promoter, a
134 promoter that is active only after glucose exhaustion. We observed that mRuby-TUB1 was
135 incorporated into the Q-nMT bundle only after phase I (Fig. 1F and Sup. Fig. 1G) confirming
136 the existence of a second wave of MT elongation in phase II. All the above information lead
137 us to propose the model presented in Fig. 1G (see figure legend).
138
139 **Q-nMT bundle formation is an active process regulated in time**
140 Increasing viscosity of the cytoplasm was shown to dampen MT dynamics (Molines et
141 al., 2022). Upon quiescence establishment, yeast cells experience a fluid phase to solid-like
142 transition (Munder et al., 2016; Joyner et al., 2016) and an acidification (Jacquel et al., 2021)
143 that could contribute to Q-nMT bundle formation. Several evidences indicate that these
144 changes in physico-chemical properties are not involved in Q-nMT formation. First, 4-day-old
145 quiescent cells can simultaneously display both dynamic cytoplasmic MTs (cMT) and a stable
146 Q-nMT bundle (Sup. Fig. 1H and (Laporte et al., 2013)). Second, when we mimicked a fluid
147 phase to solid like transition in proliferating cells by artificially dropping the pH, no stable
148 MTs were observed, while F-actin aggregation was induced (Sup. Fig. 1I) as expected from
149 (Peters et al., 2013). Third, 2-day-old quiescent cells displaying a phase III Q-nMT bundle
150 were able to grow *de novo* dynamic MTs after a pulsed-chase Noc treatment (Sup. Fig. 1J).

151 If Q-nMT bundle formation was solely depending on physico-chemical changes, this
152 structure should be able to assemble in late quiescence. By treating cells with Noc upon
153 glucose exhaustion, we managed to prevent Q-nMT bundle formation in early quiescence
154 (Fig. 1H). Strikingly, when the drug was washed out 24 h later, no Q-nMT bundle assembled,
155 even several days after Noc removal (Fig. 1H). We verified that these cells did enter
156 quiescence as they assembled actin bodies (Fig. 1H, right panel), another quiescent cell
157 specific structure (Sagot et al., 2006). This experiment strongly suggests that Q-nMT
158 formation is an active process induced by a transient signal emitted upon glucose
159 exhaustion.

160 Mutants that cannot assemble Q-nMT bundle have a reduced viability in quiescence
161 and a decreased capacity to form colonies upon quiescence exit (Laporte et al., 2013). To
162 establish a causal link between the absence of Q-nMT bundle and the above phenotypes, we
163 took advantage of our ability to prevent conditionally Q-nMT bundle formation in WT cells
164 using early Noc treatment. We demonstrated that in the absence of Q-nMT bundle, both
165 prototroph and auxotroph WT cells loose viability in quiescence and that survivors had a
166 reduced capacity to generate a progeny upon quiescence exit (Sup. Fig. 1K). This reinforce
167 the idea that the Q-nMT bundle is required for cell survival upon chronological aging.

168

169 **Tubulin steady state level and Tub3 isoform are critical for Q-nMT bundle formation.**

170 We then focused on deciphering the molecular mechanisms involved in Q-nMT
171 bundle formation. Yeast cells express two α-tubulin isotypes, Tub1 and Tub3. In proliferating
172 cells, Tub1 make up the majority (Aiken et al., 2019; Nsamba et al., 2021; Schatz et al., 1986).
173 In 4-day-old cells, both isoforms were embedded into the Q-nMT bundle (Fig. 2A and Sup.
174 Fig. 2A). As Tub3 stabilizes MTs *in vitro* (Bode et al., 2003), it may be key for Q-nMT bundle

175 formation in quiescence. To test this hypothesis, we first analyzed the phenotype of *tub3Δ*
176 cells. In phase II, *tub3Δ* cells displayed short MT bundles that were highly sensitive to Noc. In
177 phase III, no MT bundle could be detected (Fig. 2B). Thus in this mutant, MT bundles
178 assembled during phase I were not stable and ultimately collapsed. Yet, in *tub3Δ* cells, the
179 steady state amount of α-tubulin is significantly decreased (Sup. Fig. 2B and (Nsamba et al.,
180 2021)). Thus, the amount of α-tubulin, but not Tub3 itself, could be important for Q-nMT
181 bundle formation. Indeed, mutants impaired for α- and β-tubulin folding, such as the
182 prefolding complex mutants *pac10Δ*, *gim3Δ* or *yke2Δ,* or for tubulin heterodimer formation
183 such as *pac2Δ*, or for β-tubulin folding, such as *cin2Δ* or *cin4Δ*, all of which displaying a
184 decreased amount of tubulin, were unable to assemble a Q-nMT bundle (Sup. Fig. 2C-D).

185 To identify the role of Tub3 *per se*, we took advantage of the "*Tub1-only*" mutant in
186 which the *TUB3* gene was replaced by the *TUB1* gene at the *TUB3* locus. This mutant only
187 expresses Tub1 and displays an α-tubulin level similar to WT (Sup. Fig. 2B and (Nsamba et al.,
188 2021)). We found that "*Tub1-only*" cells display shorter but stable Q-nMT bundles in phase
189 III (Fig. 2C). Interestingly, "*Tub1-only*" Q-nMT bundles were thinner than WT Q-nMT bundles
190 (Fig. 2D). Overall, these data indicate Tub3 is involved in MT elongation in phase II.

191

192 **Kinetochores are critical for phase I but dispensable for the maintenance of Q-nMT**
193 **bundles.**

194 Kinetochore components are enriched at the Q-nMT bundle +end ((Laporte et al.,
195 2013) and Sup Fig. 3A). We thus wondered if kinetochore-MT attachment could play a role in
196 Q-nMT bundle formation. First, we disrupted kinetochore-MT attachment upon phase I
197 using the well-established *ndc80-1* allele (Cheeseman et al., 2006; DeLuca et al., 2018; Wigge
198 et al., 1998). As shown in Fig. 3A, no Q-nMT bundles were detected in *ndc80-1* cells shifted

199 to 37°C at the onset of quiescence entry. Second, we focused on the chromosomal
200 passenger complex (CPC: Bir1/Survivin, Sli15/INCENP, Nbl1/Borealin and Ipl1/Aurora B), a
201 complex known to regulate kinetochore-MT attachment dynamics (Cairo and Lacefield,
202 2020). We found that upon quiescence entry, Ipl1 inactivation impeded MT bundle
203 formation (Fig. 3B). While we could not detect Ipl1 and Ndc1 in quiescent cells, we found
204 that Sli15-GFP and Bir1-GFP localized along the Q-nMT bundle with an enrichment at the Q-
205 nMT bundle +end (Fig. 3C). The deletion of Sli15 did not affect Q-nMT bundle (Fig. Sup. 3E).
206 However, in 4-days old *bir1Δ* cells, Q-nMT bundle length were slightly shorter and not fully
207 stabilized (Fig. 3D). Finally, we investigated the involvement of Bim1, a MT +end binding
208 protein that plays a role in kinetochore MT-end on attachment (Dudziak et al., 2021; Thomas
209 et al., 2016). We have previously shown that Bim1 localizes all along the Q-nMT bundle but
210 that its deletion has no impact on Q-nMT bundle formation even in the presence of Noc
211 ((Laporte et al., 2013) and Fig. 3D). Interestingly, the amount of Bim1 was correlated with
212 tubulin incorporation during Q-nMT bundle formation (Sup Fig. 3D). When we combined
213 *bim1Δ* with *bir1Δ,* cells hardly assembled MT structures that vanished after Noc treatment
214 (Fig. 3D). This demonstrates that in the absence of Bim1, Bir1 was critical for Q-nMT bundle
215 stabilization in phase I. A similar phenotype was observed with *SLI15* deletion (Sup Fig. 3E).
216 Interestingly, the viability of *bim1Δ bir1Δ* cells in quiescence was drastically reduced (Sup Fig.
217 3G). Together, these experiments show that kinetochore-MT attachments are critical for the
218 initiation of Q-nMT bundle assembly.

219 We then hypothesized that inter-kinetochore interactions may stabilize the parallel
220 MTs embedded into the Q-nMT bundle. To test this idea, we analyzed MT organization in
221 s*lk19Δ* cells that are defective in kinetochore clustering (Richmond et al., 2013). In
222 quiescence, Slk19 was enriched at both Q-nMT bundle extremities (Fig. 3E). s*lk19Δ* cells

223 displayed shorter and thinner MT structures that were not stable, i.e. sensitive to Noc
224 treatmant (Fig. 3F). Since Bim1 has been involved in kinetochore-kinetochore interaction, we
225 combined s*lk19Δ* with *bim1Δ.* MT structures detected in s*lk19Δ bim1Δ* cells hardly reached
226 ≈1 µm and vanished upon Noc treatment. In addition, kinetochores localized as a rosette
227 around the SPB (Fig. 3F) and cell viability was strongly compromised (Sup. Fig. 3G). This
228 demonstrates that in the absence of Bim1, Slk19 is strictly essential for MT bundling and
229 stabilization in phase I. Furthermore, since kinetochores are known to be cross-linked by the
230 monopolin complex (Mam1, Lrs4, Hrr25 and Csm1 (Corbett et al., 2010)) we analyzed the
231 phenotype of *mam1Δ, lrs4Δ* and *csm1Δ* cells in quiescence. Most of them displayed short MT
232 structures often arranged in a star-like array (Fig. 3G-H, Sup. Fig. 3F). As for Bir1 and Skl19,
233 the combination of *bim1* deletion with monopolin disruption worsens MT structure length
234 and stability (Fig. 3H) and the cell viability was strongly compromised (Sup. Fig. 3G). Cells
235 impaired for Spo13, a protein involved in monopolin recruitment to kinetochores (Lee et al.,
236 2004) displayed a similar phenotype (Fig. 3G-H). Altogether, these experiments show that
237 inter-kinetochore interactions are critical for Q-nMT bundle assembly.

238 Lastly, we investigated if kinetochore-MT interactions were required for Q-nMT
239 bundle stability once it is formed. In 5-days old WT cells, we used a UV-pulsed-laser to break
240 the Q-nMT bundle into two pieces (Fig. 3I). The presence of dynamic cMTs after laser
241 ablation testified for cell viability (Fig. 3I). In most cases, the length of both the released
242 fragment and the fragment attached to the SPB remained constant (Fig. 3I, Sup. Fig. 3H). By
243 contrast, in proliferating cells, dynamic anaphase spindles promptly disassembled following
244 a pulse-laser break (Sup. Fig. 3I). This demonstrates that once Q-nMT bundles are formed,
245 they do not need MT-kinetochore interaction to be maintained. Accordingly, Ndc80 or Ipl1
246 inactivation in cells that are already in quiescence had no effect on the Q-nMT bundle

247 maintenance (Sup. Fig. 3B-C). Importantly, the above experiment indicates that once
248 formed, Q-nMT stability is established and maintained throughout its length.
249
250
251 **Specific kinesins are required for each step of Q-nMT bundle formation**
252 To go further in the deciphering of the molecular mechanism involved in Q-nMT
253 bundle formation, we focused on kinesins. Kar3 is a kinesin that, in complex with its
254 regulator Cik1, can generate parallel MT bundles from a MT organizing center (MTOC) both
255 *in vitro* and in proliferative cells (Manning et al., 1999; Mieck et al., 2015; Molodtsov et al.,
256 2016). In quiescence, we found that Kar3-3GFP localized at the SPB, but also as dots along
257 the Q-nMT bundle (Fig. 4A). In 4 day-old *kar3Δ* cells, the majority of the detected MT
258 structures were extremely short compared to WT (Fig. 4B and Sup Fig. 4A). Same results
259 were obtained in *cik1Δ* but not in *vik1Δ* cells, which lack the alternate Kar3 regulators (Fig.
260 4B). Thus, the Kar3/Cik1 complex is required for phase I.
261 Cin8 is a Kinesin-5 that cross-links MTs (Bodrug et al., 2020; Pandey et al., 2021; Singh
262 et al., 2018), and as such, could play a role in Q-nMT bundle stabilization. Cin8 was hardly
263 detectable in quiescent cells (Sup. Fig. 4B) and *cin8Δ* cells assembled Q-nMT bundles that
264 were thinner than in WT cells (Fig. 4C-E). Yet, these thinner bundles became stabilized in
265 phase III (Fig. 4C and Sup. Fig. 4C-D). Overall, these results strongly suggest that Cin8 is
266 required for phase II MT nucleation and/or elongation but not for stabilization in phase III.
267 Yeast have an additional Kinesin-5 called Kip1 (Fridman et al., 2013). In quiescence,
268 most of the Kip1-GFP signal was observed at the Q-nMT bundle +end (Fig. 4F). In *kip1Δ* cells,
269 phase I was slightly delayed and Q-nMT bundle were not stabilized in phase III (Fig. 4G-H),
270 yet they were as thick as WT Q-nMT bundles (Sup. Fig. 4E). These data demonstrate that

271 Kip1 is required for Q-nMT bundle stabilization in phase III. Of note, in phase I and II, Q-nMT
272 bundles were slightly longer in cells deleted for the Kinesin-8 Kip3, a MT depolymerase
273 ((Fukuda et al., 2014) Fig. 4 G-H and Sup. Fig. 4G) but were unaffected in cells deleted for
274 Kip2, a kinesin that stabilizes cytoplasmic MTs ((Hibbel et al., 2015) Sup. Fig. 4F-G). Taken
275 together our results demonstrate that each phase of Q-nMT bundle assembly involves
276 specific kinesins.
277
278 **Q-nMT bundle disassembly conditions SPB duplication/separation**
279 Finally, we questioned the molecular mechanism of Q-nMT bundle disassembly upon
280 quiescence exit. Cycloheximide prevented Q-nMT bundle disassembly indicating that this
281 process requires *de novo* protein synthesis (Fig. 5A). We then measured Q-nMT bundle
282 thickness upon depolymerization, and found that while Q-nMT bundles shortened, they did
283 not get thinner (Fig. 5B). In agreement, Nuf2-GFP clusters found at the Q-nMT bundle +end
284 moved back to the SPB while the Nuf2-GFP clusters localized in the middle of the structure
285 remained immobile until they are reached by these later (Sup. Fig. 5 A). This shows that all
286 the MT +ends did not start depolymerizing at the same time, and that longer MTs
287 depolymerized first. This finding is in agreement with our model in which MTs are cross-
288 linked all along the Q-nMT bundle length.
289 Since Kip3 is the only well-characterized yeast MT depolymerase, we studied Q-nMT
290 bundle disassembly in *kip3Δ* cells and observed that it was drastically delayed (Fig. 5C), yet
291 its overall depolymerization rate remained unaffected (Sup. Fig. 5B). In fact, we found that in
292 WT cells, Kip3 needs to be resynthesized upon quiescence exit (Fig. 5D). We searched for
293 proteins that could be involved in Q-nMT bundle disassembly together with Kip3. Among
294 proteins required for mitotic spindle disassembly, we found that inactivation of *CDC14*,

295 *CDC15*, *CDH1*, *DCC1* and *TOR1* had no effect on Q-nMT bundle disassembly, just as with the
296 inactivation of Ipl1 or proteins involved in kinetochore-MT attachment (Sup. Fig. 5 C to F).
297 The sole additional actor we found was She1, a dynein regulator (Bergman et al., 2012),
298 which deletion strongly aggravated the *kip3Δ* phenotype (Fig. 5C). Thus, Q-nMT bundle
299 disassembly does not rely on the canonical mitotic spindle disassembly machinery but,
300 rather, specifically required Kip3 and She1.

301 Importantly, when we followed quiescence exit at the individual cell level, Q-nMT
302 bundle depolymerization always preceded SPB duplication/separation (Fig. 5A) and thus, in
303 both WT and in *kip3Δ* cells (Fig. 5E, F). In fact, when we impeded Q-nMT bundle disassembly
304 using *kip3Δ she1Δ*, we found that SPB duplication was severely delayed (Fig. 5G-H, Sup. Fig.
305 5G-H). Importantly, *kip3Δ she1Δ* cells proliferated just like WT cells (Sup. Fig. 5G) and upon
306 quiescence exit, these mutant cells disassembled actin bodies just as in WT cells (Sup. Fig.
307 5I), demonstrating that *kip3Δ she1Δ* cells were not impaired in sensing quiescent exit signals.
308 These observations indicate that Q-nMT bundle has to be disassembled to allow SPB
309 duplication/separation upon quiescence exit and cell cycle re-entry.

310 **Discussion**

311 Our results shed light on the precise temporal sequences that generate a Q-nMT
312 bundle upon quiescence establishment in yeast. From bacteria to human stem cells,
313 modifications of the cell physico-chemical properties are known to accompany quiescence
314 establishment. Among these modifications, a reduction of the cellular volume increases
315 molecular crowding (Joyner et al., 2016) and pH acidification causes changes in the surface
316 charges of macromolecules and viscosity increases (Charruyer and Ghadially, 2018; Jacquel
317 et al., 2021; Munder et al., 2016; Persson et al., 2020). Much evidence points to these
318 modifications as a trigger for the auto-assembly of several types of enzyme-containing
319 granules (Munder et al., 2016; Petrovska et al., 2014; Rabouille and Alberti, 2017), or
320 complex structures such as P-bodies and Proteasome Storage Granules (Peters et al., 2013;
321 Jacquel et al., 2021; Currie et al., 2023). Recently, Molines and colleagues showed that
322 cytoplasmic viscosity modulates MT dynamics *in vivo* (Molines et al., 2022). Here, we show
323 that Q-nMT bundle formation does not rely on modifications of the physicochemical
324 properties that cells experience upon quiescence establishment (Sup. Fig. 1). In fact,
325 dynamic cMTs and a stable Q-nMT bundle can be observed simultaneously in a quiescent
326 cell (Sup. Fig. 1H), while physicochemical properties evolve in parallel both in the nucleus
327 and in the cytoplasm (Joyner et al., 2016). Importantly, reduction of the cellular volume, pH
328 acidification and increased viscosity are observed within minutes upon glucose starvation
329 (Joyner et al., 2016) while the Q-nMT bundle needs a couple of days to be fully assembled
330 (Fig. 1A). Further, we show that its formation cannot be delayed in time (Fig. 1H) and as such
331 probably depends on an active process induced by a transient signal emitted upon glucose
332 exhaustion. We speculate that the SPB may act as a platform that integrates this signal, and
333 transfers it to the MT machinery in order to assemble a stable parallel structure.

334 As it is required for the onset of Q-nMT bundle formation (Fig. 3B), Aurora B/Ilp1, a
335 kinase that plays a key role at the MT-kinetochore interface where it senses tension, could
336 be one of the target of the above-mentioned nutritional signal. In parallel, upon quiescence
337 establishment, chromosomes hyper-condensation (Guidi et al., 2015; Rutledge et al., 2015)
338 may modify tension at the kinetochore/MT interface and as such could contribute to the
339 initiation of phase I. Besides, Bim1 has also been involved in MT-kinetochore attachment
340 (Dudziak et al., 2021; Akhmanova and Steinmetz, 2015). Although it deletion alone has no
341 effect on Q-nMT bundle formation, its role become critical for phase I if kinetochore-MT
342 interaction are already destabilized by the absence of other CPC components such as Sli15
343 and Bir1 (Fig. 3D and Sup. Fig. 3E). Altogether, these observations point to kinetochore-MT
344 interaction as essential for phase I initiation, as confirmed by the absence of Q-nMT bundle
345 in the *ndc80-1* mutant (Fig. 3A).

346 In phase I, SPB-anchored MTs elongate and are concomitantly stabilized (Fig. 1 A-C).
347 This step requires the kinesin-14 Kar3 and its regulator Cik1 (Fig. 4B). During mating
348 (Molodtsov et al., 2016), and in early mitosis, when half-spindles form (Kornakov et al.,
349 2020), Kar3/Cik1, together with Bim1, align and cross-link growing MTs along existing ones,
350 thereby promoting the organization of MTs into parallel bundles. Yet, in mitosis, the kinesin-
351 14/EB1 complex promotes MT dynamics (Kornakov et al., 2020). In phase I, whether the
352 robust MT stabilization depends on the modification of the kinesin-14/EB1 complex
353 properties or is due to additional specific cross-linker(s) remains to be clarified (Fig. 6b).

354 In quiescence, deletion of either monopolin or Slk19 leads to the formation of short,
355 shattered and flared MT structures, phenotypes that are worsened by the deletion of Bim1
356 (Fig. 3F-H and Sup. Fig. 3F). Since Monopolin and Slk19 are involved in kinetochore clustering
357 (Plowman et al., 2019; Rabitsch et al., 2003; Tóth et al., 2000; Lee et al., 2004; Mittal et al.,

358 2019; Movshovich et al., 2008; Richmond et al., 2013; Zeng et al., 1999), we speculate that
359 kinetochore-kinetochore interaction may not only help preventing depolymerization of
360 single MT, but also constrain elongating phase I MTs and facilitate their concomitant cross-
361 linking (Fig. 6c).

362 With the initiation of phase I, Tub4 starts accumulating at the SPB to allow the
363 second wave of MT nucleation observed in phase II. When phase II MTs elongate, they are
364 concurrently stabilized along pre-existing phase I MTs (Fig. 6d). This step relies on the
365 kinesin-5/Cin8 as Q-nMT bundles assembled in *cin8Δ* cells are thinner than WT Q-nMT
366 bundles (Fig. 4C and D). Intriguingly, *in vitro,* the monomeric form of the vertebrate kinesin-5
367 Eg5 promotes MT nucleation and stabilizes lateral tubulin-tubulin contacts (Chen et al 2019).
368 We thus assume that in the absence of Cin8, either nucleation of phase II MTs cannot occur,
369 or phase II MTs can elongate, but cannot be cross-linked and stabilized to phase I MT while
370 they grow, and as such rapidly vanish. An absence of bundle thickening in phase II is also
371 observed in the "*Tub1-only*" mutant *i.e.* in the absence of Tub3. Tubulin isoforms or tubulin
372 PTM can allow the recruitment of specific kinesins and thereby modify MT properties, see
373 for example (Sirajuddin et al., 2014; Peris et al., 2009; Dunn et al., 2008). May Tub3 be
374 important for Cin8 recruitment or function during phase II?

375 Then, MTs elongate, but their distal parts (>1 µm) are not yet stable (Fig. 1A). The
376 full-length Q-nMT bundle stabilization is reached about 2 days after glucose exhaustion. This
377 step depends on the kinesin-5/Kip1 (Fig. 4 G-H and Sup. Fig. 4E) that is essential to cross-link
378 and stabilize elongating MTs during phase III (Fig. 6e). Accordingly, we observed a Kip1
379 enrichment at the Q-nMT bundle +ends (Fig. 4F). Thus, in agreement with their ability to
380 form homo-tetramers able to cross-link (Acar et al., 2013; Kapitein et al., 2005; Scholey et
381 al., 2014; Weinger et al., 2011) and stabilize parallel MTs (Kapitein et al., 2005; Shimamoto

382 et al., 2015; Yukawa et al., 2020), the two yeast kinesin 5 are essential for Q-nMT bundle
383 formation. Yet, in quiescence, just as in mitosis, Kip1 and Cin8 have clearly non-equivalent
384 functions (Roostalu et al., 2011; Shapira and Gheber, 2016).

385 So far, our results indicate that the Q-nMT bundle formation mechanism is different
386 from the one at work during mitotic spindle assembly. Similarly, we show that Q-nMT bundle
387 disassembly relies on a mechanism that does not involves the same pathway than mitotic
388 spindle dismantlement. Indeed, Q-nMT bundle disassembly involves Kip3 (Fig. 5C-D) but is
389 independent of the anaphase-promoting complex and Aurora B (Woodruff et al., 2010).
390 Interestingly, the longest MTs start depolymerizing from their +ends first. Then, when they
391 reach the +ends of shorter MTs, they embark them on depolymerization (Sup. Fig. 5A). This
392 cooperative behavior has been observed *in vitro* within parallel MT bundles (Laan et al.,
393 2008) and our data indicate that such a comportment can exist *in vivo*. In telophase, the CPC
394 localizes to the end of the two half-spindles in order to participate in mitotic spindle
395 disassembly (Ibarlucea-Benitez et al., 2018). Intriguingly, in quiescence, CPC is poised at the
396 Q-nMT bundle + end (Fig. 3C). May this CPC localization facilitate Q-nMT bundle rapid
397 disassembly once environmental conditions become favorable, thus ensuring quiescence
398 exit efficiency?

399 Finally, in the present study, we show that the Q-nMT bundle is required for WT cells
400 survival in quiescence. While we do not yet know why this structure is important to face
401 chronological age, it is clear that the presence of Q-nMT bundle strongly alters the nuclear
402 organization (Laporte et al., 2013; Laporte and Sagot, 2014; Laporte et al., 2016). As
403 chromatin organization influences gene expression, one hypothesis could be that the
404 presence of Q-nMT bundle is required for expression of genes required for cell survival in
405 quiescence. Another attractive hypothesis could be that the Q-nMT bundle is the yeast

406 analog of the primary cilium of mammalian cells. In fact, these two structures formed upon
407 proliferation cessation, they are both composed of highly stable parallel MTs, their
408 formation involve MT motors, and they are both template from the centriole/SPB. More
409 importantly, we show here that the Q-nMT disassembly is needed to authorize nascent SPB
410 separation upon quiescence exit (Fig. 5). Thus, the Q-nMT bundle disassembly may controls
411 reentry into the proliferation cycle, just as the primary cilium does in ciliated mammalian
412 cells (Goto et al., 2017; Kim and Tsiokas, 2011).

413 ## Materiel and Methods

414 **Yeast strains, plasmids and growth conditions**

415 All the strains used in this study are isogenic to BY4741 (*mat a, leu2Δ0, his3Δ0, ura3Δ0,*
416 *met15Δ0)* or BY4742 (*mat alpha, leu2Δ0, his3Δ0, ura3Δ0, lys2Δ0),* available from GE
417 Healthcare Dharmacon Inc. (UK), except in Fig. 2, in which S288c strains were used (Nsamba
418 et al., 2021). BY strains carrying GFP fusions were obtained from ThermoFisher Scientific
419 (Waltham, MA, USA). Integrative plasmid p*Tub1-mTurquoise2-Tub1*, p*Tub1-wasabi-Tub1*,
420 p*Tub1-mRUBY2-Tub1*, p*Tub1-mEOS2-Tub1* were a generous gift of Wei-Lih Lee (Markus et
421 al., 2015). The strain expressing SPC42-mRFP1 is a generous gift from E. O'Shea (Huh et al.,
422 2003). The strain expressing TUB4-mTQZ is generous gift of S. Jaspersen (Burns et al., 2015).
423 Three copies of eGFP in tandem were integrated at the 3' end of *DAD2*, *TUB3* or *KAR3*
424 endogenous loci respectively. Plasmids for expressing Nup2-RFP (p3695) or Bim1-3xGFP
425 (p4587) from the endogenous locus were described in (Laporte et al., 2013).
426 For Fig. 1F, *pHIS3:mTurquoise2-Tub1+3'UTR::LEU2* was integrated at *TUB1* locus, then a
427 pRS303-*ADH2p-mRuby2-Tub1* was integrated at the *HIS3* locus. To generate this plasmid, the
428 *ADH2* promoter was amplified from yeast genomic DNA flanked with NotI and SpeI
429 restrictions sites and inserted in pRS303. The mRuby2-Tub1+3'UTR, including the 116-
430 nucleotide intron and 618 nucleotides downstream the stop codon was cloned between
431 SpeI/SalI sites.
432 Yeast cells were grown in liquid YPDA medium at 30 °C in flasks as described previously in
433 (Sagot et al., 2006) except for experiments using thermosensitive strains, where cells were
434 first grown at 25 °C then shifted at 37 °C for indicated time before imaging.
435 Experiment in Sup. Fig. 1I was performed as described in (Orij et al., 2009, Peters et al.,
436 2013). In brief, proliferating cells were transfered at an OD_{600nm} of 0.5 in Hepes buffer (25

437 mM Hepes, pH 7.4, 200 mM KCl, 1 mM $CaCl_2$, and 2% dextrose) buffered either at pH 4 or
438 7.5, in the presence of 100 µM CCCP (Sigma-Aldrich). After 150 min 30 °C shaking, cells were
439 imaged (for mTQZ-Tub1) or fixed and stained using Alexa Fluor 568–phalloidin (Invitrogen) as
440 described (Sagot et al., 2006).
441 For live cell imaging, 2 µL of the cell culture were spotted onto a glass slide and immediately
442 imaged at room temperature.
443 For quiescence exit, cells were then incubated 2-3 min in liquid YPD and a 2 µL were spread
444 onto a 2 % agarose microscope pad containing YPD. Individual cells were imaged every hour,
445 up to 6 or 12 h at 21°C. For quiescence exit in presence of cycloheximide (Fig. 5A), cells were
446 pre-incubated 30 min in the presence of the drug prior quiescence exit. Cycloheximide was
447 used at 180 µM (Sigma-Aldrich), Nocodazole was used at 30 µg/mL (7.5 µM) (Sigma-Aldrich).

448 **Fluorescence Microscopy**

449 Cells were observed on a fully-automated Zeiss 200M inverted microscope (Carl Zeiss,
450 Thornwood, NY, USA) equipped with an MS-2000 stage (Applied Scientific Instrumentation,
451 Eugene, OR, USA), a Lambda LS 300 Watt xenon light source (Sutter, Novato, CA, USA), a
452 100X 1.4NA Plan-Apochromat objective, and a 5 position filter turret. For RFP imaging we
453 used a Cy3 filter (Ex: HQ535/50 nm – Em: HQ610/75 nm – BS: Q565 nm lp). For GFP imaging,
454 we used a FITC filter (excitation, HQ487/25 nm; emission, HQ535/40 nm; beam splitter,
455 Q505 nm lp). For mTurquoise imaging we used a DAPI filter (Ex: 360/40 nm – Em: 460/50
456 nm– BS: 400 nm). All the filters are from Chroma Technology Corp. Images were acquired
457 using a CoolSnap HQ camera (Roper Scientific, Tucson, AZ, USA). The microscope, camera,
458 and shutters (Uniblitz, Rochester, NY, USA) were controlled by SlideBook software 5. 0.
459 (Intelligent Imaging Innovations, Denver, CO, USA).

460 For PALM (Fig. 4E) a Nikon Ti-Eclipse equipped with iLas2 TIRF arm, laser diodes (405, 488,
461 532, 561, 642 nm), a 100x 1.49 oil (TIRF) objective connected to a EMCCD Camera
462 Photometrics Evolve was used.
463 Immunofluorescence was done as in (Laporte et al. 2015), using AlexaFluor Phalloidin
464 (Invitrogen).
465 For expansion microscopy (Sup Fig. 2A), spheroplasts were obtained as described in (Laporte
466 et al., 2016). After washes in 10 mg/mL NaBH4 in PEMS for 10 min, spheroplasts were
467 seeded on 12 mm round poly-L-lysine coated coverslips, washed twice for 30 min in 100 µL
468 PEM-BAL (PEM + 1% BSA) and incubated with the primary antibodies (anti-GFP from mouse;
469 Roche, ref. 11814460001, 1/50; anti-alpha-tubulin from rat; YOL1/34, Abcam, ref. Ab6161,
470 1/100) for 1 hour at 37°C. Cells were then washed three times in PEM-BAL and incubated
471 with the secondary antibodies (Goat anti-mouse AlexaFluor®488 1/200 and Donkey anti-rat
472 AlexaFluor®555; A11029 and A21434 respectively, ThermoFisher Scientific, Waltham, MA)
473 for 45 min at 37 °C. Cells were then washed three times with PBS. Cells were processed for
474 Expansion Microscopy as previously described in (Bahri et al., 2021). Spheroplasts were
475 incubated for 10 min in 0.25 % GA in PBS, washed in PBS three times for 5 min, and
476 processed for gelation. A drop of 100 µL of ExM MS (8.625% (wt/wt) SA, 2.5% (wt/wt) AA,
477 0.15 % (wt/wt) BIS, 2 M NaCl in 1× PBS) was placed on the chilled Parafilm, and coverslips
478 were put on the drop with cells facing the solution and incubated for 3 min. Then the
479 coverslips were transferred to a 35 µL of ExM MS supplemented with 0.2 % APS and 0.2 %
480 TEMED, with the initiator (APS) added last. Gelation proceeded for 3 min on ice, and samples
481 were incubated at 37 °C in a humidified chamber in the dark for 1 h. Then coverslips with
482 attached gels were transferred into a six-well plate for incubation in 2 mL of digestion buffer
483 (1× TAE buffer, 0.5% Triton X-100, 0.8 M guanidine hydrochloride, pH ~8.3) supplemented

484 with DAPI (1 µg/mL) for 10-15 min at 37 °C, until the gels detached. Fresh proteinase K at 8
485 units/mL was then added and samples incubated at 37 °C for 30 min. Finally, gels were
486 removed and placed in 10mL petri dishes filled with ddH2O for expansion. Water was
487 exchanged at least twice every 30 min, and incubated in ddH2O overnight at RT. Gels
488 expanded between 4× and 4.2× according to SA purity. Expanded cells were imaged with a
489 UPlanS Apo 100×/1.4 oil immersion objective in an Olympus IX81 microscope (Olympus,
490 Tokyo, Japan). For Structured illumination microscopy (SIM, Fig. 7D), a ZEISS Lattice
491 Lightsheet 7 was used.
492 Laser ablation (Fig. 3I) was performed at room temperature with a 100X oil Plan-Apochromat
493 objective lens (NA 1.4) and an Axio-Observed.Z1 microscope (Carl Zeiss) equipped with a
494 spinning disk confocal (Yokogawa), an EMCCD Evolve camera (Photometrics and Roper
495 Scientific) and 491 nm (100 mW; Cobolt calypso) and 561 nm (100 mW; Cobolt Jive) lasers.
496 Images were acquired with Metamorph software (Roper Scientific). Every 5 to 20 s, a Z-series
497 of 0.4 µm steps were acquired. A 355 nm microchip laser (Teem Photonics) with a 21 kHz
498 repetition rate, 0.8 µJ energy/pulse, 2 kW of peak power and 400 ps pulse width, powered
499 with an iLas2 PULSE system (Roper Scientific) was used between 10 to 40 % power with one
500 pulse of a spot length of 100 points. Breakage was considered as successful if a non-
501 alignment between the two remaining Q-n MT bundle fragments was observed.
502 Z-stacks were deconvolved using the Deconvolution Lab plugin (Fig. 1D; Fig. 3C,E,F Fig. 4A,F).
503 In figures 1F, 4A, B, G, supplemental figure 1H and 3B a faint and fuzzy fluorescence signal is
504 detected in some cell cytoplasm using the GFP filter set. This signal is not GFP but rather due
505 to a non-specific yellow background fluorescence.
506 **Image analysis**

507 Distribution and associated statistics were performed using GraphPad Prism 5 (GraphPad
508 Software, Inc. La Jolla, USA). Unless specified, histograms and scatter dot plots show the
509 mean and the error bars indicate SD. MT length was measured on MAX-projected image
510 using imageJ.

511 For MT fluorescence intensity measurement, a line scan (i1) of 4 pixel width containing both
512 FP signal and background was drawn along MTs on SUM projection image (3-4 Z-plans) using
513 ImageJ. A line of 8 pixels width (at the same location) was drawn in order to calculate the
514 intensity of the surrounding background (i2). The real intensity (ir) was calculated as follow:
515 int=(i1-((i2x8)-(i1x4))/4). Similar approach was conducted to measure Tub4 fluorescence
516 intensity (Fig. 1E) *i.e.* (i1) and (i2) were two boxes, the second including the first one.
517 Intensity was calculated as follow: int=[i1-([(i2xi2$_{surface}$)-(i1xi1$_{surface}$)]/(i2$_{surface}$-
518 i1$_{surface}$))*i1$_{surface}$]. For morphometric Q-nMT bundle property distribution (Fig. 1C and 4B)the
519 mean fluorescence intensity was measured in each individual cell, in a finite area localized
520 adjacent to the SPB (0,4 µm – 3-4 Z stack sum projected) as an estimate of Q-nMT bundle
521 width and plotted as a function of the according measured bundle length.

522 For Nuf2 fluorescence intensity measurement at SPB (Sup. Fig. 1D), GFP and RFP line scan
523 measurements were done on a 3-4 Z-plans sum projection. The "SPB localization zone" was
524 defined as the length ending at the second pixel after the brightest RFP signal of Spc42-RFP.
525 The remaining Q-nMT bundle zone was defined as the "+end zone". The total Nuf2-GFP
526 signal detected along the Q-nMT bundle was set to 100 % (sum projection imaged) allowing
527 to determine the percentage of the signal measured at "SPB localization zone" and at "+end
528 zone"

529 Normalized Q-nMT bundle length (Fig. 3C) was done after line scan intensity measurement.
530 mTQZ-Tub1 intensities slopes were first aligned on their inflexion point. To compare Q-nMT

531 bundle with different lengths, we first sorted Q-nMT bundle <1.8 µm. After an artificial
532 isotropic expansion, we fit all MT structures to length order. Then, corresponding mean
533 intensity of Q-nMT bundle (mTZQ-Tub1) and GFP signal were calculated.
534 To measure the Q-nMT bundle depolymerization (Fig. 5A and E), individual Q-nMT bundle
535 length were measured over time. The first measurement was set at 100 % of the length, and
536 the following percentages calculated accordingly. A fluorescence drop above or equal to 25
537 % defines the inflexion point of the slope, and was used to align the different length
538 measurements. The FWHM (Full Width at Half Maximum) was calculated by measuring
539 fluorescence intensity of a line crossing perpendicularly a Q-nMT bundle, from a sum
540 projection. After fitting intensity level with Gaussian distribution and obtained the standard
541 deviation (σ) value, FWHM was calculated using the equation $2\sqrt{(2\ln 2)}\times\sigma$. In Fig. 5B, FWHM
542 was measured at 0.5 µm of the SPB.

543 **Western blots**

544 Western blots were done as described in (Sagot et al., 2006) using anti-GFP antibodies
545 (Roche); anti-Tat1 antibodies (a generous gift from J-P. Javerzat) and antibody against the
546 budding yeast Act1 or Sac6, generous gifts from B. Goode.

547 **Phenotypical analysis of cells without Q-nMT bundle**

548 WT strains were grown to glucose exhaustion (OD ~6.5), washout with “old YPDA” and
549 pulsed with either DMSO or Nocodazole (30µg/mL) for 24 h. Cells were then washed twice in
550 “old YPDA” before being incubated in the same medium. Dead cell measurement was done
551 using methylene blue staining. The capacity of cells to exit quiescence was scored after cells
552 micro-manipulation (N=4, n>100) as described in (Laporte et al., 2011).

553

554 ## Supplemental data

555 **Supplementary Figure 1** further described the 3 steps of Q-nMT bundle formation. It shows
556 the impact of physico-chemical cell properties on MT stabilization and demonstrate that Q-
557 nMT bundle is required for both cell viability in quiescence and quiescence exit fitness.

558 **Supplementary Figure 2** describes the impact of the alpha tubulin level on Q-nMT bundle
559 assembly.

560 **Supplementary Figure 3** demonstrates that kinetochore-MT interactions are not required
561 for Q-nMT bundle maintenance and that mutants affected for kinetochore-kinetochore
562 interactions have a reduced viability in quiescence.

563 **Supplementary Figure 4** impact of various yeast kinesin deletion on Q-nMT bundle
564 morphometric parameters.

565 **Supplementary Figure 5** Q-nMT bundle disassembly in mutants affected for mitotic spindle
566 dismantlement.

567

Acknowledgments

The authors would like to thank the Bordeaux Imaging center for the help in super-resolution imaging. We also thank Zeiss for their help with SIM. We express our gratitude to E. O'Shea, S. Jaspersen, J-P. Javerzat, Wei-Lih Lee and B. Goode for sharing reagents. We would like to thank J-P. Javerzat for helpful and constructive discussions about our work. DL, AML, JD and IS were supported by a grant from the ANR-21-CE13-0023-01, a Ligue Contre le Cancer Régionale – Dordogne grant #193366 and the CNRS. MG and EN were supported by a National Science Foundation grant number MCB-1846262. AR was supported by the Conseil Régional d'Aquitaine (#20111301010) and the CNRS.

Author Contributions

D. Laporte did all the experiments described in this manuscript, except Fig. 1F, 1H, Fig. 5 G-H and Sup. Fig. 5G to I that were performed by A. Massoni-Laporte, together with all image deconvolution, and Fig. 4E and Sup. Fig. 2A and 3A that were done by J. Dompierre. A. Royou helped for pulse-laser experiments of Fig. 3I and Sup Fig. 3H-I. C. Lefranc did molecular biology and western blots. D. Mauboules performed yeast genetic for Fig. 2. M. L. Gupta Jr and E. T. Nsamba created the Tub1-only mutant (Fig. 2). L. Gal and M. Schuldiner performed high throughput deletion screen. IS and DL designed and supervised the experiments. IS and DL wrote the manuscript.

588 **References**

589 Acar, S., D.B. Carlson, M.S. Budamagunta, V. Yarov-Yarovoy, J.J. Correia, M.R. Niñonuevo, W.
590 Jia, L. Tao, J.A. Leary, J.C. Voss, J.E. Evans, and J.M. Scholey. 2013. The bipolar
591 assembly domain of the mitotic motor kinesin-5. *Nat Commun*. 4:1343.
592 doi:10.1038/ncomms2348.

593 Aiken, J., J.K. Moore, and E.A. Bates. 2019. TUBA1A mutations identified in lissencephaly
594 patients dominantly disrupt neuronal migration and impair dynein activity. *Human*
595 *Molecular Genetics*. 28:1227–1243. doi:10.1093/hmg/ddy416.

596 Akhmanova, A., and M.O. Steinmetz. 2015. Control of microtubule organization and
597 dynamics: two ends in the limelight. *Nature Reviews Molecular Cell Biology*. 16:711–
598 726. doi:10.1038/nrm4084.

599 Anvarian, Z., K. Mykytyn, S. Mukhopadhyay, L.B. Pedersen, and S.T. Christensen. 2019.
600 Cellular signalling by primary cilia in development, organ function and disease. *Nat*
601 *Rev Nephrol*. 15:199–219. doi:10.1038/s41581-019-0116-9.

602 Baas, P.W., A.N. Rao, A.J. Matamoros, and L. Leo. 2016. Stability properties of neuronal
603 microtubules. *Cytoskeleton (Hoboken)*. 73:442–460. doi:10.1002/cm.21286.

604 Bahri, H., J. Buratto, M. Rojo, J.P. Dompierre, B. Salin, C. Blancard, S. Cuvellier, M. Rose, A.
605 Ben Ammar Elgaaied, E. Tetaud, J.-P. di Rago, A. Devin, and S. Duvezin-Caubet. 2021.
606 TMEM70 forms oligomeric scaffolds within mitochondrial cristae promoting in situ
607 assembly of mammalian ATP synthase proton channel. *Biochim Biophys Acta Mol Cell*
608 *Res*. 1868:118942. doi:10.1016/j.bbamcr.2020.118942.

609 Bergman, Z.J., X. Xia, I.A. Amaro, and T.C. Huffaker. 2012. Constitutive dynein activity in She1
610 mutants reveals differences in microtubule attachment at the yeast spindle pole
611 body. *Mol Biol Cell*. 23:2319–2326. doi:10.1091/mbc.E12-03-0223.

612 Bodakuntla, S., A.S. Jijumon, C. Villablanca, C. Gonzalez-Billault, and C. Janke. 2019.
613 Microtubule-Associated Proteins: Structuring the Cytoskeleton. *Trends Cell Biol*.
614 29:804–819. doi:10.1016/j.tcb.2019.07.004.

615 Bode, C.J., M.L. Gupta, K.A. Suprenant, and R.H. Himes. 2003. The two alpha-tubulin isotypes
616 in budding yeast have opposing effects on microtubule dynamics in vitro. *EMBO Rep.*
617 4:94–99. doi:10.1038/sj.embor.embor716.

618 Bodrug, T., E.M. Wilson-Kubalek, S. Nithianantham, A.F. Thompson, A. Alfieri, I. Gaska, J.
619 Major, G. Debs, S. Inagaki, P. Gutierrez, L. Gheber, R.J. McKenney, C.V. Sindelar, R.
620 Milligan, J. Stumpff, S.S. Rosenfeld, S.T. Forth, and J. Al-Bassam. 2020. The kinesin-5
621 tail domain directly modulates the mechanochemical cycle of the motor domain for
622 anti-parallel microtubule sliding. *eLife*. 9:e51131. doi:10.7554/eLife.51131.

623 Burns, S., J.S. Avena, J.R. Unruh, Z. Yu, S.E. Smith, B.D. Slaughter, M. Winey, and S.L.
624 Jaspersen. 2015. Structured illumination with particle averaging reveals novel roles

625 for yeast centrosome components during duplication. *Elife*. 4.
626 doi:10.7554/eLife.08586.

627 Cairo, G., and S. Lacefield. 2020. Establishing correct kinetochore-microtubule attachments
628 in mitosis and meiosis. *Essays in Biochemistry*. 64:277–287.
629 doi:10.1042/EBC20190072.

630 Charruyer, A., and R. Ghadially. 2018. Influence of pH on Skin Stem Cells and Their
631 Differentiation. *Curr Probl Dermatol*. 54:71–78. doi:10.1159/000489520.

632 Cheeseman, I.M., J.S. Chappie, E.M. Wilson-Kubalek, and A. Desai. 2006. The conserved KMN
633 network constitutes the core microtubule-binding site of the kinetochore. *Cell*.
634 127:983–997. doi:10.1016/j.cell.2006.09.039.

635 Chen, G.-Y., J.M. Cleary, A.B. Asenjo, Y. Chen, J.A. Mascaro, D.F.J. Arginteanu, H. Sosa, and
636 W.O. Hancock. 2019. Kinesin-5 Promotes Microtubule Nucleation and Assembly by
637 Stabilizing a Lattice-Competent Conformation of Tubulin. *Curr Biol*. 29:2259-2269.e4.
638 doi:10.1016/j.cub.2019.05.075.

639 Cleary, J.M., and W.O. Hancock. 2021. Molecular mechanisms underlying microtubule
640 growth dynamics. *Curr Biol*. 31:R560–R573. doi:10.1016/j.cub.2021.02.035.

641 Corbett, K.D., C.K. Yip, L.-S. Ee, T. Walz, A. Amon, and S.C. Harrison. 2010. The monopolin
642 complex crosslinks kinetochore components to regulate chromosome-microtubule
643 attachments. *Cell*. 142:556–567. doi:10.1016/j.cell.2010.07.017.

644 Currie, S.L., W. Xing, D. Muhlrad, C.J. Decker, R. Parker, and M.K. Rosen. 2023. Quantitative
645 reconstitution of yeast RNA processing bodies. *Proc Natl Acad Sci U S A*.
646 120:e2214064120. doi:10.1073/pnas.2214064120.

647 DeLuca, K.F., A. Meppelink, A.J. Broad, J.E. Mick, O.B. Peersen, S. Pektas, S.M.A. Lens, and
648 J.G. DeLuca. 2018. Aurora A kinase phosphorylates Hec1 to regulate metaphase
649 kinetochore-microtubule dynamics. *J Cell Biol*. 217:163–177.
650 doi:10.1083/jcb.201707160.

651 Dudziak, A., L. Engelhard, C. Bourque, B.U. Klink, P. Rombaut, N. Kornakov, K. Jänen, F.
652 Herzog, C. Gatsogiannis, and S. Westermann. 2021. Phospho-regulated Bim1/EB1
653 interactions trigger Dam1c ring assembly at the budding yeast outer kinetochore.
654 *EMBO J*. 40:e108004. doi:10.15252/embj.2021108004.

655 Dunn, S., E.E. Morrison, T.B. Liverpool, C. Molina-París, R.A. Cross, M.C. Alonso, and M.
656 Peckham. 2008. Differential trafficking of Kif5c on tyrosinated and detyrosinated
657 microtubules in live cells. *J Cell Sci*. 121:1085–1095. doi:10.1242/jcs.026492.

658 Fridman, V., A. Gerson-Gurwitz, O. Shapira, N. Movshovich, S. Lakämper, C.F. Schmidt, and L.
659 Gheber. 2013. Kinesin-5 Kip1 is a bi-directional motor that stabilizes microtubules
660 and tracks their plus-ends in vivo. *J Cell Sci*. 126:4147–4159. doi:10.1242/jcs.125153.

661 Fukuda, Y., A. Luchniak, E.R. Murphy, and M.L. Gupta. 2014. Spatial control of microtubule
662 length and lifetime by opposing stabilizing and destabilizing functions of Kinesin-8.
663 *Curr Biol*. 24:1826–1835. doi:10.1016/j.cub.2014.06.069.

664 Goodson, H.V., and E.M. Jonasson. 2018. Microtubules and Microtubule-Associated Proteins.
665 *Cold Spring Harb Perspect Biol*. 10:a022608. doi:10.1101/cshperspect.a022608.

666 Goto, H., H. Inaba, and M. Inagaki. 2017. Mechanisms of ciliogenesis suppression in dividing
667 cells. *Cell Mol Life Sci*. 74:881–890. doi:10.1007/s00018-016-2369-9.

668 Gudimchuk, N.B., and J.R. McIntosh. 2021. Regulation of microtubule dynamics, mechanics
669 and function through the growing tip. *Nat Rev Mol Cell Biol*. 22:777–795.
670 doi:10.1038/s41580-021-00399-x.

671 Guidi, M., M. Ruault, M. Marbouty, I. Loïodice, A. Cournac, C. Billaudeau, A. Hocher, J.
672 Mozziconacci, R. Koszul, and A. Taddei. 2015. Spatial reorganization of telomeres in
673 long-lived quiescent cells. *Genome Biol.* 16:206. doi:10.1186/s13059-015-0766-2.

674 Hahn, I., A. Voelzmann, Y.-T. Liew, B. Costa-Gomes, and A. Prokop. 2019. The model of local
675 axon homeostasis - explaining the role and regulation of microtubule bundles in axon
676 maintenance and pathology. *Neural Dev*. 14:11. doi:10.1186/s13064-019-0134-0.

677 Heald, R., and A. Khodjakov. 2015. Thirty years of search and capture: The complex simplicity
678 of mitotic spindle assembly. *J Cell Biol*. 211:1103–1111. doi:10.1083/jcb.201510015.

679 Hibbel, A., A. Bogdanova, M. Mahamdeh, A. Jannasch, M. Storch, E. Schäffer, D. Liakopoulos,
680 and J. Howard. 2015. Kinesin Kip2 enhances microtubule growth in vitro through
681 length-dependent feedback on polymerization and catastrophe. *Elife*. 4:e10542.
682 doi:10.7554/eLife.10542.

683 Huh, W.-K., J.V. Falvo, L.C. Gerke, A.S. Carroll, R.W. Howson, J.S. Weissman, and E.K. O'Shea.
684 2003. Global analysis of protein localization in budding yeast. *Nature*. 425:686–691.
685 doi:10.1038/nature02026.

686 Ibarlucea-Benitez, I., L.S. Ferro, D.G. Drubin, and G. Barnes. 2018. Kinesins relocalize the
687 chromosomal passenger complex to the midzone for spindle disassembly. *J Cell Biol*.
688 217:1687–1700. doi:10.1083/jcb.201708114.

689 Jacquel, B., T. Aspert, D. Laporte, I. Sagot, and G. Charvin. 2021. Monitoring single-cell
690 dynamics of entry into quiescence during an unperturbed life cycle. *Elife*. 10:e73186.
691 doi:10.7554/eLife.73186.

692 Janke, C., and M.M. Magiera. 2020. The tubulin code and its role in controlling microtubule
693 properties and functions. *Nat Rev Mol Cell Biol*. 21:307–326. doi:10.1038/s41580-
694 020-0214-3.

695 Jin, Q., E. Trelles-Sticken, H. Scherthan, and J. Loidl. 1998. Yeast nuclei display prominent
696 centromere clustering that is reduced in nondividing cells and in meiotic prophase. *J.*
697 *Cell Biol.* 141:21–29.

698 Joyner, R.P., J.H. Tang, J. Helenius, E. Dultz, C. Brune, L.J. Holt, S. Huet, D.J. Müller, and K.
699 Weis. 2016. A glucose-starvation response regulates the diffusion of
700 macromolecules. *Elife*. 5. doi:10.7554/eLife.09376.

701 Kapitein, L.C., E.J.G. Peterman, B.H. Kwok, J.H. Kim, T.M. Kapoor, and C.F. Schmidt. 2005. The
702 bipolar mitotic kinesin Eg5 moves on both microtubules that it crosslinks. *Nature*.
703 435:114–118. doi:10.1038/nature03503.

704 Kim, S., and L. Tsiokas. 2011. Cilia and cell cycle re-entry: more than a coincidence. *Cell Cycle*.
705 10:2683–2690. doi:10.4161/cc.10.16.17009.

706 Kirschner, M., and T. Mitchison. 1986. Beyond self-assembly: from microtubules to
707 morphogenesis. *Cell*. 45:329–342.

708 Kornakov, N., B. Möllers, and S. Westermann. 2020. The EB1-Kinesin-14 complex is required
709 for efficient metaphase spindle assembly and kinetochore bi-orientation. *J Cell Biol*.
710 219. doi:10.1083/jcb.202003072.

711 Laan, L., J. Husson, E.L. Munteanu, J.W.J. Kerssemakers, and M. Dogterom. 2008. Force-
712 generation and dynamic instability of microtubule bundles. *Proc Natl Acad Sci U S A*.
713 105:8920–8925. doi:10.1073/pnas.0710311105.

714 Laporte, D., F. Courtout, B. Pinson, J. Dompierre, B. Salin, L. Brocard, and I. Sagot. 2015. A
715 stable microtubule array drives fission yeast polarity reestablishment upon
716 quiescence exit. *J. Cell Biol.* 210:99–113. doi:10.1083/jcb.201502025.

717 Laporte, D., F. Courtout, B. Salin, J. Ceschin, and I. Sagot. 2013. An array of nuclear
718 microtubules reorganizes the budding yeast nucleus during quiescence. *J. Cell Biol.*
719 203:585–594. doi:10.1083/jcb.201306075.

720 Laporte, D., F. Courtout, S. Tollis, and I. Sagot. 2016. Quiescent Saccharomyces cerevisiae
721 forms telomere hyperclusters at the nuclear membrane vicinity through a
722 multifaceted mechanism involving Esc1, the Sir complex, and chromatin
723 condensation. *Mol. Biol. Cell*. 27:1875–1884. doi:10.1091/mbc.E16-01-0069.

724 Laporte, D., and I. Sagot. 2014. Microtubules move the nucleus to quiescence. *Nucleus*.
725 5:113–118. doi:10.4161/nucl.28538.

726 Lee, B.H., B.M. Kiburz, and A. Amon. 2004. Spo13 maintains centromeric cohesion and
727 kinetochore coorientation during meiosis I. *Curr Biol*. 14:2168–2182.
728 doi:10.1016/j.cub.2004.12.033.

729 Liu, P., M. Würtz, E. Zupa, S. Pfeffer, and E. Schiebel. 2021. Microtubule nucleation: The
730 waltz between γ-tubulin ring complex and associated proteins. *Curr Opin Cell Biol*.
731 68:124–131. doi:10.1016/j.ceb.2020.10.004.

732 Manning, B.D., J.G. Barrett, J.A. Wallace, H. Granok, and M. Snyder. 1999. Differential
733 regulation of the Kar3p kinesin-related protein by two associated proteins, Cik1p and
734 Vik1p. *J Cell Biol*. 144:1219–1233. doi:10.1083/jcb.144.6.1219.

735 Markus, S.M., S. Omer, K. Baranowski, and W.-L. Lee. 2015. Improved Plasmids for
736 Fluorescent Protein Tagging of Microtubules in Saccharomyces cerevisiae. *Traffic*.
737 16:773–786. doi:10.1111/tra.12276.

738 Meiring, J.C.M., B.I. Shneyer, and A. Akhmanova. 2020. Generation and regulation of
739 microtubule network asymmetry to drive cell polarity. *Curr Opin Cell Biol*. 62:86–95.
740 doi:10.1016/j.ceb.2019.10.004.

741 Mieck, C., M.I. Molodtsov, K. Drzewicka, B. van der Vaart, G. Litos, G. Schmauss, A. Vaziri,
742 and S. Westermann. 2015. Non-catalytic motor domains enable processive
743 movement and functional diversification of the kinesin-14 Kar3. *eLife*. 4:e04489.
744 doi:10.7554/eLife.04489.

745 Mitchison, T., and M. Kirschner. 1984. Dynamic instability of microtubule growth. *Nature*.
746 312:237–242.

747 Mittal, P., A. Chavan, D. Trakroo, S. Shah, and S.K. Ghosh. 2019. Outer kinetochore protein
748 Dam1 promotes centromere clustering in parallel with Slk19 in budding yeast.
749 *Chromosoma*. 128:133–148. doi:10.1007/s00412-019-00694-9.

750 Molines, A.T., J. Lemière, M. Gazzola, I.E. Steinmark, C.H. Edrington, C.-T. Hsu, P. Real-
751 Calderon, K. Suhling, G. Goshima, L.J. Holt, M. Thery, G.J. Brouhard, and F. Chang.
752 2022. Physical properties of the cytoplasm modulate the rates of microtubule
753 polymerization and depolymerization. *Developmental Cell*. 57:466-479.e6.
754 doi:10.1016/j.devcel.2022.02.001.

755 Molodtsov, M.I., C. Mieck, J. Dobbelaere, A. Dammermann, S. Westermann, and A. Vaziri.
756 2016. A Force-Induced Directional Switch of a Molecular Motor Enables Parallel
757 Microtubule Bundle Formation. *Cell*. 167:539-552.e14.
758 doi:10.1016/j.cell.2016.09.029.

759 Movshovich, N., V. Fridman, A. Gerson-Gurwitz, I. Shumacher, I. Gertsberg, A. Fich, M.A.
760 Hoyt, B. Katz, and L. Gheber. 2008. Slk19-dependent mid-anaphase pause in kinesin-
761 5-mutated cells. *J Cell Sci*. 121:2529–2539. doi:10.1242/jcs.022996.

762 Munder, M.C., D. Midtvedt, T. Franzmann, E. Nüske, O. Otto, M. Herbig, E. Ulbricht, P.
763 Müller, A. Taubenberger, S. Maharana, L. Malinovska, D. Richter, J. Guck, V.
764 Zaburdaev, and S. Alberti. 2016. A pH-driven transition of the cytoplasm from a fluid-
765 to a solid-like state promotes entry into dormancy. *eLife*. 5:e09347.
766 doi:10.7554/eLife.09347.

767 Muroyama, A., and T. Lechler. 2017. Microtubule organization, dynamics and functions in
768 differentiated cells. *Development*. 144:3012–3021. doi:10.1242/dev.153171.

769 Nsamba, E.T., A. Bera, M. Costanzo, C. Boone, and M.L. Gupta Jr. 2021. Tubulin isotypes
770 optimize distinct spindle positioning mechanisms during yeast mitosis. *Journal of Cell*
771 *Biology*. 220:e202010155. doi:10.1083/jcb.202010155.

772 Pandey, H., M. Popov, A. Goldstein-Levitin, and L. Gheber. 2021. Mechanisms by Which
773 Kinesin-5 Motors Perform Their Multiple Intracellular Functions. *Int J Mol Sci*.
774 22:6420. doi:10.3390/ijms22126420.

775 Peris, L., M. Wagenbach, L. Lafanechère, J. Brocard, A.T. Moore, F. Kozielski, D. Job, L.
776 Wordeman, and A. Andrieux. 2009. Motor-dependent microtubule disassembly
777 driven by tubulin tyrosination. *J Cell Biol*. 185:1159–1166.
778 doi:10.1083/jcb.200902142.

779 Persson, L.B., V.S. Ambati, and O. Brandman. 2020. Cellular Control of Viscosity Counters
780 Changes in Temperature and Energy Availability. *Cell*. 183:1572-1585.e16.
781 doi:10.1016/j.cell.2020.10.017.

782 Peters, L.Z., R. Hazan, M. Breker, M. Schuldiner, and S. Ben-Aroya. 2013. Formation and
783 dissociation of proteasome storage granules are regulated by cytosolic pH. *J. Cell Biol.*
784 201:663–671. doi:10.1083/jcb.201211146.

785 Petrovska, I., E. Nüske, M.C. Munder, G. Kulasegaran, L. Malinovska, S. Kroschwald, D.
786 Richter, K. Fahmy, K. Gibson, J.-M. Verbavatz, and S. Alberti. 2014. Filament
787 formation by metabolic enzymes is a specific adaptation to an advanced state of
788 cellular starvation. *Elife*. doi:10.7554/eLife.02409.

789 Plowman, R., N. Singh, E.C. Tromer, A. Payan, E. Duro, C. Spanos, J. Rappsilber, B. Snel,
790 G.J.P.L. Kops, K.D. Corbett, and A.L. Marston. 2019. The molecular basis of monopolin
791 recruitment to the kinetochore. *Chromosoma*. 128:331–354. doi:10.1007/s00412-
792 019-00700-0.

793 Rabitsch, K.P., M. Petronczki, J.P. Javerzat, S. Genier, B. Chwalla, A. Schleiffer, T.U. Tanaka,
794 and K. Nasmyth. 2003. Kinetochore recruitment of two nucleolar proteins is required
795 for homolog segregation in meiosis I. *Dev Cell*. 4:535–548. doi:10.1016/s1534-
796 5807(03)00086-8.

797 Rabouille, C., and S. Alberti. 2017. Cell adaptation upon stress: the emerging role of
798 membrane-less compartments. *Curr Opin Cell Biol*. 47:34–42.
799 doi:10.1016/j.ceb.2017.02.006.

800 Richmond, D., R. Rizkallah, F. Liang, M.M. Hurt, and Y. Wang. 2013. Slk19 clusters
801 kinetochores and facilitates chromosome bipolar attachment. *Mol Biol Cell*. 24:566–
802 577. doi:10.1091/mbc.E12-07-0552.

803 Roll-Mecak, A. 2020. The Tubulin Code in Microtubule Dynamics and Information Encoding.
804 *Dev Cell*. 54:7–20. doi:10.1016/j.devcel.2020.06.008.

805 Roostalu, J., C. Hentrich, P. Bieling, I.A. Telley, E. Schiebel, and T. Surrey. 2011. Directional
806 Switching of the Kinesin Cin8 Through Motor Coupling. *Science*.
807 doi:10.1126/science.1199945.

808 Roostalu, J., and T. Surrey. 2017. Microtubule nucleation: beyond the template. *Nat. Rev.*
809 *Mol. Cell Biol.* doi:10.1038/nrm.2017.75.

810 Röper, K. 2020. Microtubules enter centre stage for morphogenesis. *Philos Trans R Soc Lond*
811 *B Biol Sci*. 375:20190557. doi:10.1098/rstb.2019.0557.

812 Rutledge, M.T., M. Russo, J.-M. Belton, J. Dekker, and J.R. Broach. 2015. The yeast genome
813 undergoes significant topological reorganization in quiescence. *Nucleic Acids Res.*
814 43:8299–8313. doi:10.1093/nar/gkv723.

815 Sagot, I., B. Pinson, B. Salin, and B. Daignan-Fornier. 2006. Actin bodies in yeast quiescent
816 cells: an immediately available actin reserve? *Mol. Biol. Cell*. 17:4645–4655.
817 doi:10.1091/mbc.E06-04-0282.

818 Sanchez, A.D., and J.L. Feldman. 2017. Microtubule-organizing centers: from the centrosome
819 to non-centrosomal sites. *Curr. Opin. Cell Biol.* 44:93–101.
820 doi:10.1016/j.ceb.2016.09.003.

821 Schatz, P.J., F. Solomon, and D. Botstein. 1986. Genetically essential and nonessential alpha-
822 tubulin genes specify functionally interchangeable proteins. *Mol Cell Biol*. 6:3722–
823 3733. doi:10.1128/mcb.6.11.3722-3733.1986.

824 Scholey, J.E., S. Nithianantham, J.M. Scholey, and J. Al-Bassam. 2014. Structural basis for the
825 assembly of the mitotic motor Kinesin-5 into bipolar tetramers. *Elife*. 3:e02217.
826 doi:10.7554/eLife.02217.

827 Shapira, O., and L. Gheber. 2016. Motile properties of the bi-directional kinesin-5 Cin8 are
828 affected by phosphorylation in its motor domain. *Sci Rep*. 6:25597.
829 doi:10.1038/srep25597.

830 Shimamoto, Y., S. Forth, and T.M. Kapoor. 2015. Measuring Pushing and Braking Forces
831 Generated by Ensembles of Kinesin-5 Crosslinking Two Microtubules. *Dev Cell*.
832 34:669–681. doi:10.1016/j.devcel.2015.08.017.

833 Singh, S.K., H. Pandey, J. Al-Bassam, and L. Gheber. 2018. Bidirectional motility of kinesin-5
834 motor proteins: structural determinants, cumulative functions and physiological
835 roles. *Cell. Mol. Life Sci.* 75:1757–1771. doi:10.1007/s00018-018-2754-7.

836 Sirajuddin, M., L.M. Rice, and R.D. Vale. 2014. Regulation of microtubule motors by tubulin
837 isotypes and post-translational modifications. *Nat Cell Biol*. 16:335–344.
838 doi:10.1038/ncb2920.

839 Thawani, A., and S. Petry. 2021. Molecular insight into how γ-TuRC makes microtubules. *J*
840 *Cell Sci*. 134:jcs245464. doi:10.1242/jcs.245464.

841 Thomas, G.E., K. Bandopadhyay, S. Sutradhar, M.R. Renjith, P. Singh, K.K. Gireesh, S. Simon,
842 B. Badarudeen, H. Gupta, M. Banerjee, R. Paul, J. Mitra, and T.K. Manna. 2016. EB1
843 regulates attachment of Ska1 with microtubules by forming extended structures on
844 the microtubule lattice. *Nat Commun*. 7:11665. doi:10.1038/ncomms11665.

845 Tóth, A., K.P. Rabitsch, M. Gálová, A. Schleiffer, S.B. Buonomo, and K. Nasmyth. 2000.
846 Functional genomics identifies monopolin: a kinetochore protein required for

847 segregation of homologs during meiosis i. *Cell*. 103:1155–1168. doi:10.1016/s0092-
848 8674(00)00217-8.

849 Weinger, J.S., M. Qiu, G. Yang, and T.M. Kapoor. 2011. A nonmotor microtubule binding site
850 in kinesin-5 is required for filament crosslinking and sliding. *Curr Biol*. 21:154–160.
851 doi:10.1016/j.cub.2010.12.038.

852 Wheway, G., L. Nazlamova, and J.T. Hancock. 2018. Signaling through the Primary Cilium.
853 *Frontiers in Cell and Developmental Biology*. 6.

854 Wigge, P.A., O.N. Jensen, S. Holmes, S. Souès, M. Mann, and J.V. Kilmartin. 1998. Analysis of
855 the Saccharomyces spindle pole by matrix-assisted laser desorption/ionization
856 (MALDI) mass spectrometry. *J. Cell Biol.* 141:967–977.

857 Winey, M., and K. Bloom. 2012. Mitotic spindle form and function. *Genetics*. 190:1197–1224.
858 doi:10.1534/genetics.111.128710.

859 Woodruff, J.B., D.G. Drubin, and G. Barnes. 2010. Mitotic spindle disassembly occurs via
860 distinct subprocesses driven by the anaphase-promoting complex, Aurora B kinase,
861 and kinesin-8. *J Cell Biol*. 191:795–808. doi:10.1083/jcb.201006028.

862 Yukawa, M., Y. Teratani, and T. Toda. 2020. How Essential Kinesin-5 Becomes Non-Essential
863 in Fission Yeast: Force Balance and Microtubule Dynamics Matter. *Cells*. 9:E1154.
864 doi:10.3390/cells9051154.

865 Zeng, X., J.A. Kahana, P.A. Silver, M.K. Morphew, J.R. McIntosh, I.T. Fitch, J. Carbon, and W.S.
866 Saunders. 1999. Slk19p is a centromere protein that functions to stabilize mitotic
867 spindles. *J Cell Biol*. 146:415–425. doi:10.1083/jcb.146.2.415.

868

869 **Abbreviations**

870 MT: microtubule

871 SPB: spindle pole body

872 GTP: guanosine triphosphate

873 MTOC: microtubule organizing centers

874 ɣ-TuC: ɣ-tubulin complex

875 MAPs: microtubule associated proteins

876 Q-nMT bundle: quiescence specific nuclear microtubule bundle

877 CPC : chromosome passenger complex

878

879 ## Figure legends

880 **Figure 1: The formation of the Q-nMT bundle is a three-step process.**

881 **(A)** Nuclear MT length in WT cells expressing mTQZ-Tub1, before (grey) or after a 15 min Noc
882 treatment (blue) upon entry into quiescence.

883 **(B)** MT fluorescence intensity was used as a proxy of Q-nMT bundle width in WT cells
884 expressing mTQZ-Tub1*;* thin line: intensity of an individual cell; bold line: mean intensity;
885 n>60 for each phase. Mean intensity measurement for half pre-anaphase mitotic spindles
886 (purple) phase I (green), phase II (orange) or phase III (red) Q-nMT bundle. To help
887 comparison, in each graph, the dash line indicate the mean intensity in half pre-anaphase
888 mitotic spindle. Representative cells are shown (images in pseudo-colors).

889 **(C)** Morphometric Q-nMT bundle property distribution (length and width) in each phase
890 before and after a 15 min Noc treatment in WT cells expressing mTQZ-Tub1.

891 **(D)** Single WT cells expressing mTQZ-Tub1 (red) and Nuf2-GFP (green) in phase II (23h) or
892 phase III (50h) were deposited on an agarose pad containing Noc and imaged. Blue
893 arrowheads: SPB; white arrows: Nuf2-GFP clusters; time is in min after pad deposition**.**

894 **(E)** Tub4-mTQZ fluorescence intensity measured at the SPB upon entry into quiescence.
895 Representative cells are shown (images in pseudo-colors). Bar is 1µm

896 **(F)** WT cells expressing mTQZ-Tub1 (red) under the *TUB1* promoter and mRuby-Tub1 (green)
897 under the *ADH2* promoter. Representative cells at the indicated time after glucose
898 exhaustion and the associated line-scans are show. The graph shows the percentage of cells
899 harboring both mTQZ and mRuby fluorescence along the Q-nMT bundle. Each circle is the
900 percentage obtained for an independent cell culture, n>200).

901 **(G)** Schematic of the Q-nMT bundle formation. During phase I, stable MTs (green) elongate
902 from the SPB (in grey). During phase II, new MTs (orange) elongated from the SPB and are
903 stabilized along the phase I MTs, but stay dynamic when longer than phase I MTs. In the
904 meantime, Tub4 (blue) increases at the SPB (grey). After phase III, all MTs are stable (red).
905 **(H)** Upon glucose exhaustion, WT cells expressing mTQZ-Tub1 (green) and Nuf2-GFP (red)
906 were pulsed treated with Noc (blue) or DMSO (grey) for 24 h. Noc or DMSO were then
907 chased using carbon exhausted medium and cells were imaged. Representative images of
908 cells 2 d after the chase are shown. Right panel: same experiment done in WT prototroph
909 cells and representative images of cells 4 d after the chase are shown. Tubulin (green) was
910 detected by immunofluorescence, actin (red) by phalloidin and DNA (blue) with DAPI. The
911 mean Q-nMT bundle length (±SD) in the population is indicated.
912 In A, C, E an H, each circle corresponds to a single cell. In A, E, F and H mean and SD are
913 shown, and unpaired T-test p-values are indicated; ***: p-value<10^{-5}. In A, D, F and H bar is
914 2µm.
915
916 **Figure 2: Q-nMT bundle formation is influenced by the alpha-tubulin amount and isoform**
917 **(A)** WT cell (4 d) expressing either Tub3-3GFP (green) and mTQZ-Tub1 (red, top panel) or
918 Tub3-RFP (red) and mWasabi-Tub1 (green, bottom panel). Blue arrowheads point to SPB.
919 **(B)** Nuclear MT length in WT and *tub3Δ* cells expressing mTQZ-Tub1, 36 h (phase II, yellow)
920 and 90 h (phase III, red) after glucose exhaustion, treated 15 min (blue) or not (grey) with
921 Noc. Representative images are shown on the right.
922 **(C)** Nuclear MT length in WT and *Tub1-only* cells expressing mTQZ-Tub1, 36 h (phase II,
923 yellow) and 90 h (phase III, red) after glucose exhaustion, treated 15 min or not with Noc.
924 Representative images are shown on top.

925 **(D)** Fluorescence intensity along the Q-nMT bundle in WT (grey) and *Tub1-only* (blue) cells
926 expressing mTQZ-Tub1 grown for 10 h (phase I), 36 h (phase II), and 90 h (phase III). Thin
927 lines indicate individual cells fluorescence intensity and bold lines, the mean intensity.
928 Dashed lines indicate the maximal mean fluorescence intensity measured in phase I.
929 In B and C, each circle corresponds to a single cell. MT mean length, SD, and unpaired T-test
930 p-value are indicated. In all panels, bar is 2µm.
931
932 **Figure 3: Kinetochore-kinetochore interactions are required for Q-nMT bundle formation.**
933 **(A)** Nuclear MT length distribution in WT (grey) and *ndc80-1* (violet) cells expressing mTQZ-
934 Tub1 (green) and Nuf2-GFP (red), shifted to 37 °C upon glucose exhaustion for the indicated
935 time and imaged after a 20 min Noc treatment. Representative cells shifted for 12 h at 37°C
936 are shown.
937 **(B)** WT (grey) and *ipl1-1* cells (pink) expressing mTQZ-Tub1 were shifted upon glucose
938 exhaustion to 37 °C for 48 h, and imaged after a 20 min Noc treatment. Representative cells
939 are shown.
940 **(C)** WT cells (2 d) expressing mTQZ-Tub1 (red) and Bir1-GFP or Sli15-GFP (green) were
941 imaged. Graphs show Bir1-GFP or Sli15-GFP fluorescence intensity along normalized Q-nMT
942 bundles (plain and dash lines: mean and SD respectively).
943 **(D)** Nuclear MT length distribution in cells of the indicated genotype (4 d) expressing mTQZ-
944 Tub1 treated or not with Noc. Representative cells are shown.
945 **(E)** WT cells expressing mTQZ-Tub1 (red) and Slk19-GFP (green) 4 h after glucose exhaustion.
946 Blue arrowhead: SPB.

947 **(F)** Nuclear MT length distribution in cells of the indicated genotype (4 d) expressing mTQZ-
948 Tub1 (green) and Nuf2-GFP (red) were imaged before or after Noc treatment.
949 Representative cells are shown. White arrowheads point to Nuf2 dots.
950 **(G)** Cells of the indicated genotype (4 d) expressing mTQZ-Tub1 (green) and Nup2-RFP (red).
951 **(H)** Nuclear MT length distribution in cells of the indicated genotype (4 d) expressing mTQZ-
952 Tub1 treated or not with Noc. Representative cells are shown.
953 **(I)** Length variation of nuclear MT bundle fragments after laser ablation (pink dash line) in
954 cells expressing mRuby-TUB1 (red) and Dad2-GFP (green). Time is in min. Blue arrowhead:
955 SPB, white arrowhead: cMT.
956 In A, B, D, F, and H, each circle corresponds to a single cell. Mean, SD, and unpaired T-test p-
957 values are indicated (*: p-value <0.05, and ***: p-value <10^{-6}). Bar is 2 µm except in (I) where
958 it is 1 µm.
959
960 **Figure 4: Each phase of Q-nMT formation requires a specific kinesin.**
961 **(A)** Images and corresponding line scans of WT cells (2 d) expressing Kar3-3GFP (green) and
962 mTQZ-Tub1 (red).
963 **(B)** Morphometric Q-nMT bundle properties distribution in 4 d WT (grey), *kar3Δ* (red), *vik1Δ*
964 (blue), *cik1Δ* cells (green) expressing mTQZ-Tub1 after Noc treatment. Blue crosses are SD.
965 Each circle corresponds to an individual Q-nMT bundle. Representative cells are shown.
966 **(C)** Nuclear MT length distribution in WT and *cin8Δ* cells expressing mTQZ-Tub1 treated
967 (dashed boxes) or not (plain boxes) with Noc.
968 **(D)** Fluorescence intensity along Q-nMT bundle in WT and *cin8Δ* cells expressing mTQZ-Tub1
969 7 h and 24 h after glucose exhaustion. Representative cells are shown.

970 **(E)** WT and *cin8Δ* cells expressing mEOS3.2-Tub1 were imaged using PALM (images are in
971 pseudo-colors). Full width at half maximum (FWHM) was measured at the indicated distance
972 from the SPB. Each line in the bottom graph corresponds to a single cell. P-value between
973 WT and *cin8Δ* are indicated (unpaired T-test).
974 **(F)** WT cells (3 d) expressing Kip1-GFP (green) and mTQZ-Tub1 (red). Graphs show
975 fluorescence intensity along normalized Q-nMT bundles (plain and dash lines: mean and SD
976 respectively).
977 **(G-H)** Representative images and nuclear MT length distribution in WT, *kip1Δ* and *kip3Δ* cells
978 expressing mTQZ-Tub1 treated (dashed boxes) or not (plain boxes) with Noc.
979 In C and H, *: p-value <0.05, and ***: p-value $<10^{-6}$ (unpaired T-test). Means and SD are
980 indicated. In A, B, D, E, F and G, bar is 2 µm.
981
982 **Figure 5: Q-nMT bundle disassembly always occurs before SPB separation upon quiescence**
983 **exit.**
984 **(A)** WT cells expressing Spc42-RFP (red) and Nuf2-GFP (green) (5 d) were re-fed on an YPDA
985 microscope pad. Individual Q-nMT bundles were measured in cells treated with CHX (blue,
986 Stu2-GFP) or with DMSO alone (grey, Nuf2-GFP). Each line corresponds to an individual cell.
987 For each cell, time was set to zero at the onset of MT bundle depolymerization (black dashed
988 line).
989 **(B)** Q-nMT bundle length (green) and fluorescence intensity at full width half maximum
990 (FWHM - orange) were measured upon quiescence exit in WT cells (5 d) expressing mTQZ-
991 Tub1. Representative example of shirking Q-nMT bundle is shown on the left.

992 **(C)** Cells of the indicated genotype expressing mTQZ-Tub1 were grown for 4 d, and re-fed. Q-
993 nMT bundle length was measured at the indicated time points, 15 min after a Noc
994 treatment.

995 **(D)** Western blot (GFP antibodies) on total protein extracts from WT cells expressing Kip3-
996 GFP grown for the indicated time. Sac6 was used as a loading control (Sac6 antibodies).

997 **(E)** WT and *kip3Δ* cells (5 d) expressing Nuf2-GFP were re-fed on an YPDA microscope pad.
998 Each line corresponds to an individual cell. For each cell, time was set to zero at the onset of
999 SPB separation.

1000 (**F**) Representative images of *kip3Δ* cells expressing Nuf2-GFP upon quiescence exit. White
1001 arrowheads: Q-nMT bundle extremities.
1002 (**G**) Percentage of cells expressing Spc42-mRFP1 with separated SPB as a function of time
1003 upon quiescence exit.
1004 (**H**) WT and *kip3Δshe1Δ* cells (6 d) expressing Spc42-mRFP1 (red) and mTQZ-Tub1 (green)
1005 were re-fed on a YPDA microscope pad. Percentage of cells with a single or a duplicated SPB
1006 in the presence or absence of Q-nMT bundle were scored. Representative cells are shown.
1007 Right bottom panel: actin (phalloidin staining, red) in *kip3Δ she1Δ* cells (6 d) expressing
1008 mTQZ-Tub1 (green) before and 1 h after quiescence exit.
1009 In F and H, blue arrowheads: SPB. In all panels, bar is 2 µm.
1010

1011 **Figure 6: Model for Q-nMT bundle assembly**
1012 MT-kinetochore interaction and Ilp1 (Aurora B) are required for the onset of phase I. Kar3
1013 (kinesin-14) and its regulator Cik1 are essential to initiate Q-nMT bundle elongation.
1014 Although deletion of *BIM1* (EB1) has no effect, it becomes critical for phase I if kinetochore-

1015 MT interactions are already destabilized by the absence of Chromosome Passenger Complex
1016 components. Kinetochore clustering by the monopolin complex and Slk19 is needed to
1017 maintain MT bundling while phase I MTs elongate. During phase I, Tub4 (γ-Tubulin)
1018 accumulates at the SPB. In phase II, a second wave of MT nucleation and elongation occur.
1019 Phase II MTs are concurrently stabilized along pre-existing phase I MTs, in a Cin8 (kinesin-5)-
1020 dependent manner. Phase I and phase II MTs + end (>1 µm) remain dynamic until the full
1021 length Q-nMT bundle stabilization is reached via the action of Kip1 (kinesin-5), about 2 days
1022 after glucose exhaustion.

1023

1024 ## Supplementary Figure legends

1025 **Supplementary Figure 1**

1026 **(A)** Fluorescence intensity along MT structures in WT cells expressing mTQZ-Tub1. Pink,
1027 green and orange lines display respectively the half-mitotic spindle, phase I and phase II Q-
1028 nMT bundles. Individual cell (thin line) and mean (bold line) fluorescence intensities are
1029 shown, and the dash line indicate the according maximum fluorescence mean intensity.

1030 **(B)** Individual Q-nMT bundle full width measured at half-maximum in WT cells (4 d)
1031 expressing mTQZ-Tub1 before or after 1 h after Noc treatment. A paired T-test was use to
1032 compare the two conditions.

1033 **(C)** Nuclear MT length distribution in WT haploid (mat a and mat α) or diploid (mat a/mat α)
1034 cells expressing mTQZ-TUB1. Each circle is an individual cell.

1035 **(D)** Single WT cells expressing Nuf2-GFP (green) and Spc42-RFP (red) upon entry into
1036 quiescence. The percentages indicate the relative amount of Nuf2-GFP detected at the SBP.

1037 **(E)** Tub4-mTQZ fluorescence intensity in WT cells of the W303 background. Unpaired T-test
1038 p-values are indicated; ***: p-value<10^{-5}.

1039 **(F)** Fluorescence intensities in WT cells (4 d) expressing Tub4-mTQZ and mRuby-Tub1. The
1040 Tub4-mTQZ signal at the SBP is plotted in function of the mRuby signal along the Q-nMT
1041 bundle.

1042 **(G)** Others examples of cells expressing pTUB1-mTQZ-Tub1 (red) and pADH2-mRuby-Tub1
1043 (green) imaged in phase II.

1044 **(H)** WT cells expressing mRuby-Tub1 (4 d) can display both dynamic cMTs (red arrowhead)
1045 and a Q-nMT bundle (time is in min).

1046 **(I)** An artificial fluid phase to solid-like transition in proliferating cells does not induce MT
1047 stabilization. Proliferating WT cells expressing mTQZ-Tub1 (green) and Spc42-RFP (red) with
1048 fluid (pH=7.5) or solid like (pH=4) cytoplasm/nucleoplasm (see materials and method) were
1049 incubated 15 min with Noc (left) or stained with phalloidin (right). Indicated phenotypes
1050 were quantified (left and right graphs, N=2, n>200).
1051 **(J)** Cells can assemble dynamic cMTs (red arrowhead) in quiescence. MTs were followed in
1052 individual 2-day-old WT cells after a 15 min Noc pulse-chased (time is in min). Red
1053 arrowhead: cytoplasmic MT.
1054 **(K)** Left two graphs: WT cell viability after a pulse with Noc (blue circles) or DMSO (white
1055 triangles) for 24 h upon glucose exhaustion, then a chase using carbon exhausted medium.
1056 Each circle/triangle is an independent cell culture, n>200. Black line is the mean value of Noc
1057 and DMSO treated cells. Time is in days after the initial 24 h pulse. Right graph and images:
1058 same as previously, but 8 days after the pulse, cells were micro-separated and allowed to
1059 give rise to a colony on a YPDA plate. Each measure is the % obtained for an independent
1060 cell culture (n>100). Pictures of representative plates after 3 d of growth at 30°C are shown.
1061 In D and G, bar is 1 µm; in H, I and J, bar is 2 µm. In D and J, blue arrowhead points to the
1062 SBP.
1063
1064 **Supplementary Figure 2**
1065 **(A)** Expansion microscopy image of WT cell (4 d) expressing Tub3-3GFP and immuno-stained
1066 with GFP (green) and α-tubulin (red) YOL1/2 antibodies.
1067 **(B)** Western blot using α-tubulin YOL1/2 antibody on total protein extracts from the
1068 indicated cells grown for 4 d. Actin is the loading reference. Numbers indicate the
1069 tubulin/actin ratio (mean, N=8).

1070 **(C)** Nuclear MT length distribution in *yke2Δ*, *pac10Δ* or *gim3Δ* cells (4 d) and in
1071 corresponding WT cells expressing Nuf2-GFP (dark grey bars) or Bim1-3GFP (light grey bars).
1072 Right panel: western blot using an anti-α-tubulin antibody on total protein extracts from
1073 cells of the indicated genotype (4 d). Actin is a loading reference. The tubulin/actin ratio is
1074 indicated (N=4).
1075 **(D)** MT length distribution in *pac2Δ*, *cin2Δ* or *cin4Δ* cells (4 d). Same legend as (C).
1076 In all panels, bar is 2 µm.
1077
1078 **Supplementary Figure 3**
1079 **(A)** Upper panel: WT cell (4 d) expressing Dad2-GFP and immuno-stained with GFP (green)
1080 and α-tubulin (red) YOL1/2 antibodies imaged using expansion microscopy. Blue is DAPI.
1081 Lower panel: WT cell (4 d) expressing Dad2-GFP (green) and mRuby-Tub1 (red), imaged using
1082 SIM. Bar: 1 µm.

1083 **(B-C)** Inactivation of Ndc80 (B) or Ipl1 (C) in quiescent cells does not affect Q-nMT bundle.
1084 Nuclear MT length in cells of the indicated genotypes, grown for 3 d at 25 °C, shifted either
1085 24 h *(ndc80-1*) or 48 h (*ipl1-1*) to 37 °C and treated 15 min or not with Noc. Each circle is an
1086 individual cell, representative images are shown. Unpaired T-test p-values are indicated.
1087 Mean and SD are indicated.

1088 **(D)** Distribution of Bim1-3GFP intensity in function of mTQZ-TUB1 intensity in individual Q-
1089 nMT bundles (green: phase I – 7 h after glucose exhaustion, orange: phase II – 26 h after
1090 glucose exhaustion and red: phase III – 50h after glucose exhaustion). Each circle is an
1091 individual Q-nMT bundle.

1092 **(E)** Nuclear MT length in *bim1Δ, sli15Δ, sli15Δ bim1Δ* cells (5 d) expressing mTQZ-Tub1
1093 treated or not with Noc. Each circle is an individual cell. Mean and SD are indicated.

1094 **(F)** Percentage of cells of the indicated background displaying a MT star-like array. Each circle
1095 represents the % obtained for an independent culture (n>200). Mean and SD are indicated.

1096 **(G)** Viability after the indicated time in quiescence (left graph), capacity to form colony after
1097 20 days in quiescence (CFU, middle panel) or capacity to form a colony after single cell
1098 micro-manipulation after 12 days in quiescence (right graph). Pictures of representative
1099 plates 3 d after cell micro-manipulation are shown.

1100 **(H)** WT cells (6 d) expressing mRuby-Tub1 (red) and Nuf2-GFP (green) were transferred onto
1101 an agarose pad. Q-nMT bundles were cut using a pulsed laser (pink dashed line). Time is in
1102 min

1103 **(I)** Proliferating cells expressing mRuby-Tub1 (red) and Dad2-GFP (green) were transferred
1104 onto an agarose pad. Anaphase spindles were cut and the behavior of the released
1105 fragments was followed. White arrowheads point to dynamic cMTs. Time is in min. in A and
1106 H, blue arrowhead: SPB. Bar: 2 µm. For B, C, E-F.

1107

1108 **Supplementary Figure 4**

1109 **(A)** Morphometric Q-nMT bundle properties distribution in WT (grey) and *kar3Δ* cells (red)
1110 90 h after glucose exhaustion (control for Fig. 4B).

1111 **(B)** WT cells expressing mTQZ-Tub1 (red) and Cin8-GFP (green) were imaged at the indicated
1112 times after glucose exhaustion. Cells expressing only mTQZ-Tub1 (left panel) testify for the
1113 absence of fluorescence leak from the mTQZ signal into the GFP channel. Bar is 2µm.

1114 **(C)** Fluorescence intensity along Q-nMT bundles in WT (black) and *cin8Δ* cells expressing
1115 mTQZ-Tub1, treated (green) or not (red) with Noc. Each line is an individual cell, the bold
1116 lines are the mean.
1117 **(D)** Morphometric Q-nMT bundle properties distribution in WT (grey) and *cin8Δ* (green) cells
1118 expressing mTQZ-Tub1. Each circle is an individual cell.
1119 **(E)** Fluorescence intensity along Q-nMT bundles in WT (grey), *kip1Δ* (red), *bim1Δ* (green),
1120 and *kip1Δ bim1Δ* (blue) cells (4 d). Each line is an individual cell, the bold lines are the mean.
1121 **(F)** Nuclear MT length distribution in *kip2Δ* cells expressing mTQZ-Tub1, treated (dashed box,
1122 blue dots) or not (plain boxes, black dots) with Noc. For a comparison, the mean WT length
1123 is indicated as dashed line. Unpaired T-test p-values are indicated.
1124 **(G)** Q-nMT bundle length distribution in cells of the indicated genotype (4 d), treated (grey)
1125 or not (light blue) with Noc.
1126
1127 **Supplementary Figure 5**
1128 **(A)** Individual quiescence exit of two representative 5-day-old cells (left and right) expressing
1129 mTQZ-Tub1 (red) and Nuf2-GFP (green). Blue arrowhead: SBP; white arrows Nuf2 cluster.
1130 Time is in min.
1131 **(B)**. Q-nMT bundle disassembly in WT (grey) and in *kip3Δ* (blue). The time was set to zero at
1132 the onset MT depolymerisation. WT cells expressing Spc42-RFP and Stu2-GFP were grown 5
1133 d, then re-fed on YPDA pads and imaged every 20 min
1134 **(C-D)** Q-nMT bundle length in cells of the indicated genotype expressing mTQZ-Tub1, grown
1135 for 4 d and imaged at the indicated time after refeeding. For the rapamycin experiment, WT
1136 cells were pre-incubated 1 h with rapamycin (1 µg/mL), and then re-fed in presence of the
1137 drug. For thermos-sensitive strains (D), cells were grown 4 d at 25 °C, shifted 1 h at 37 °C,

1138 and then transferred to new medium at 37 °C to trigger quiescence exit. Measurements
1139 were done after a 15 min Noc treatment. Each circle is an individual cell.
1140 **(E-F)** WT and cells of the indicated genotype expressing mTQZ-Tub1 were grown for the
1141 indicated time at 25 °C, shifted to 37 °C and re-fed. In E, measurements were done after a 15
1142 min Noc treatment. Each circle is an individual cell.
1143 **(G)** Percentage of cells with separated SPBs upon quiescence exit on YPDA agarose pad (left
1144 panel). Right: proliferation of WT and *kip3Δshe1Δ* strains in YPDA (OD600nm as function of
1145 time).
1146 **(H)** Q-nMT bundle length distribution in WT (grey) or *kip3Δshe1Δ* (green) cells with
1147 unseparated SPBs, 240 min after quiescence exit.
1148 **(I)** Actin (red, Phalloidin-staining) in WT and *kip3Δshe1Δ* cells expressing mTQZ-TUB1 (green)
1149 at the indicated time upon quiescence exit.
1150 In C-F, red lines indicated mean intensity and SD. In A and I, bar is 2µm.
1151
1152

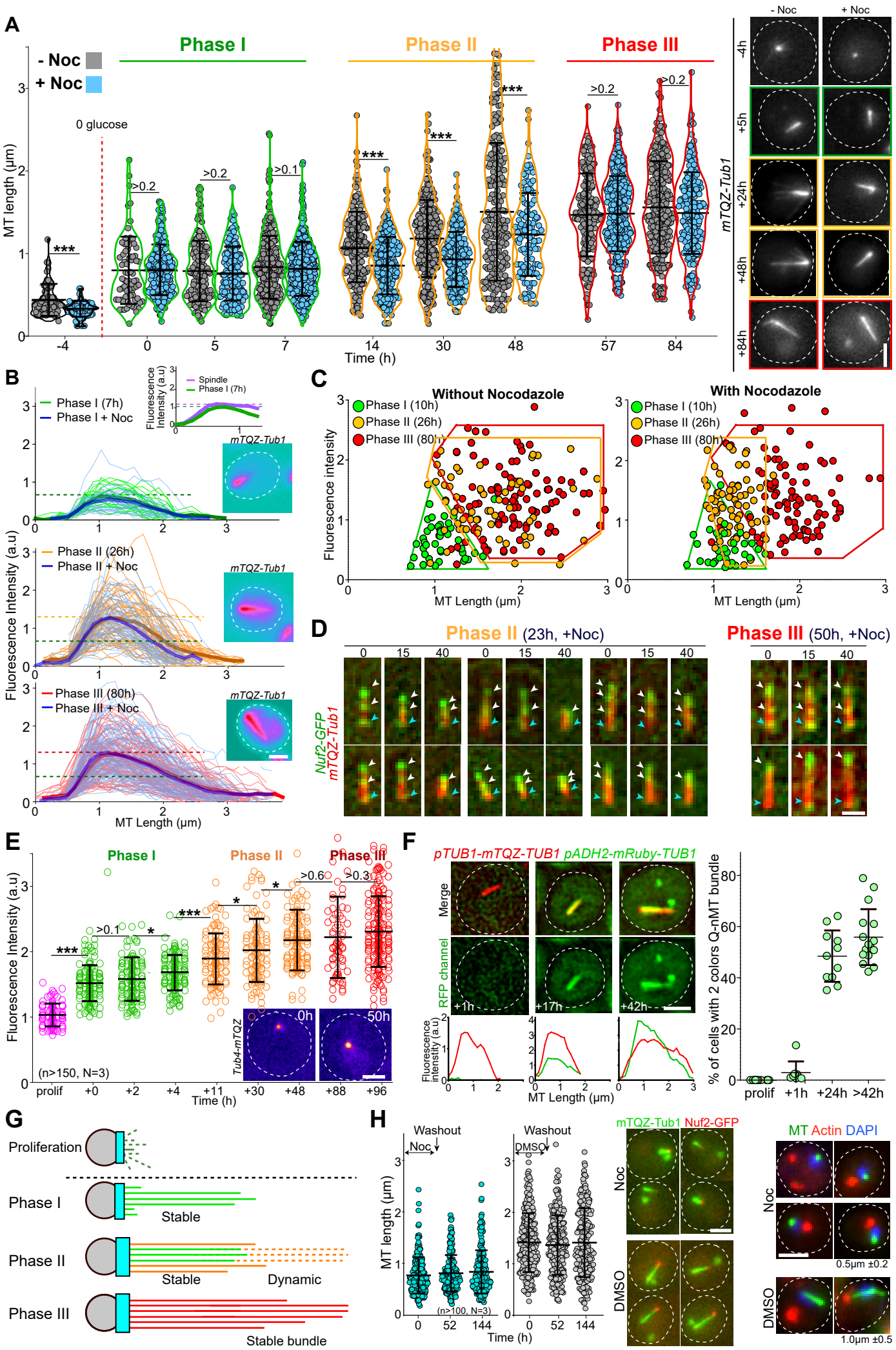
A
Phase I
Phase II
Phase III
- Noc
+ Noc
0 glucose
MT length (µm)
Time (h)
mTQZ-Tub1
B
Phase I (7h)
Phase I + Noc
Phase II (26h)
Phase II + Noc
Phase III (80h)
Phase III + Noc
Fluorescence Intensity (a.u)
MT Length (µm)
Spindle
Phase I (7h)
C
Without Nocodazole
With Nocodazole
Phase I (10h)
Phase II (26h)
Phase III (80h)
Fluorescence intensity
MT Length (µm)
D
Phase II (23h, +Noc)
Phase III (50h, +Noc)
Nuf2-GFP
mTQZ-Tub1
E
Phase I
Phase II
Phase III
Fluorescence Intensity (a.u)
(n>150, N=3)
Tub4-mTQZ
Time (h)
F
pTUB1-mTQZ-TUB1 pADH2-mRuby-TUB1
Merge
RFP channel
MT Length (µm)
% of cells with 2 colors Q-nMT bundle
G
Proliferation
Phase I
Stable
Phase II
Stable
Dynamic
Phase III
Stable bundle
H
Washout
Noc
DMSO
MT length (µm)
(n>100, N=3)
Time (h)
mTQZ-Tub1 Nuf2-GFP
MT Actin DAPI
0.5µm ±0.2
1.0µm ±0.5

Figure 1

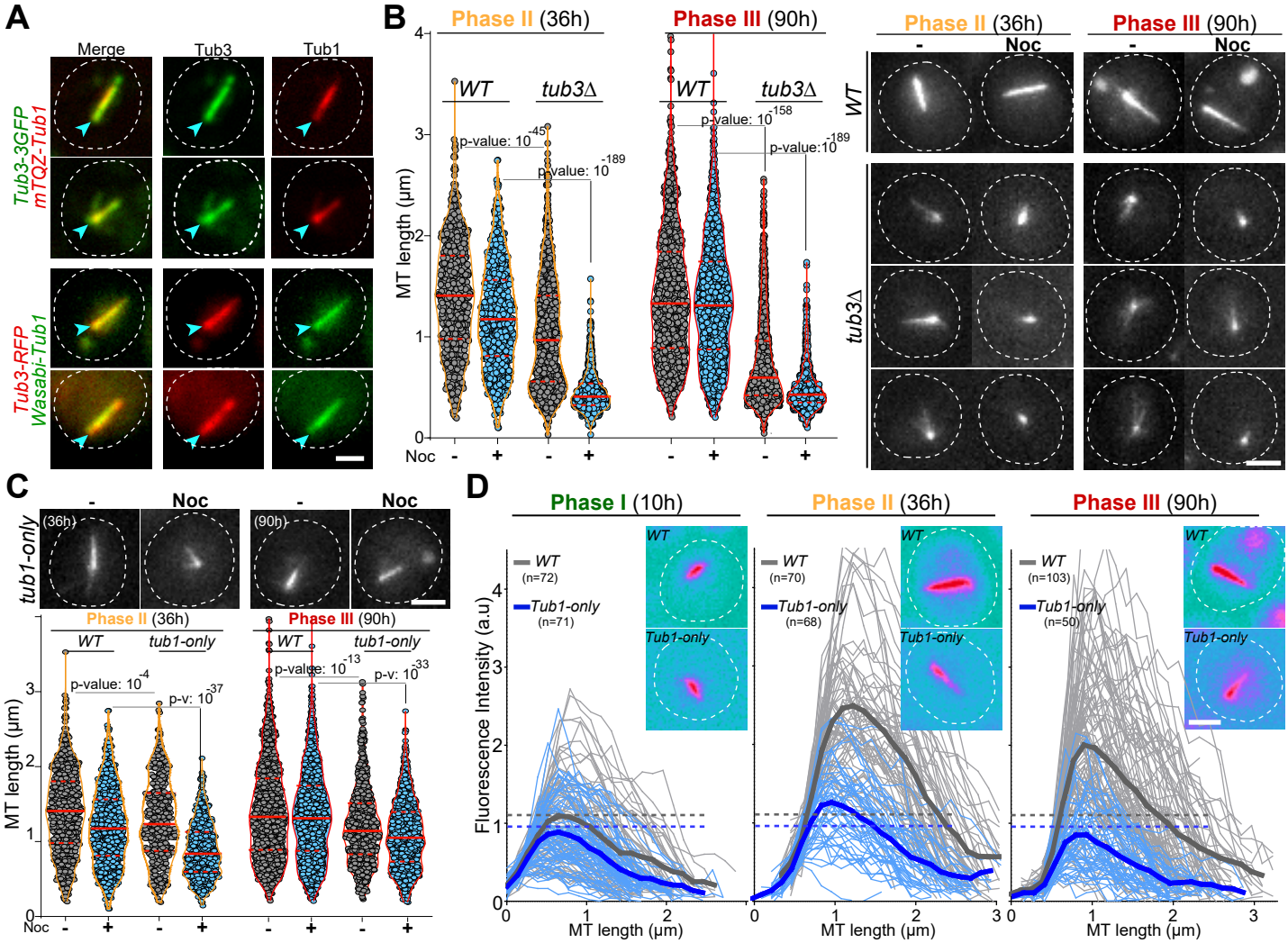
A
Merge
Tub3
Tub1
Tub3-3GFP
mTQZ-Tub1
Tub3-RFP
Wasabi-Tub1
B
Phase II (36h)
Phase III (90h)
WT
tub3Δ
p-value: 10^-45
p-value: 10^-189
p-value: 10^-158
p-value:10^-189
MT length (µm)
Noc
Phase II (36h)
Phase III (90h)
-
Noc
WT
tub3Δ
C
tub1-only
(36h)
(90h)
Phase II (36h)
Phase III (90h)
WT
tub1-only
p-value: 10^-4
p-v: 10^-37
p-value: 10^-13
p-v: 10^-33
MT length (µm)
Noc
D
Phase I (10h)
Phase II (36h)
Phase III (90h)
WT
(n=72)
Tub1-only
(n=71)
(n=70)
(n=68)
(n=103)
(n=50)
Fluorescence Intensity (a.u)
MT length (µm)

Figure 2

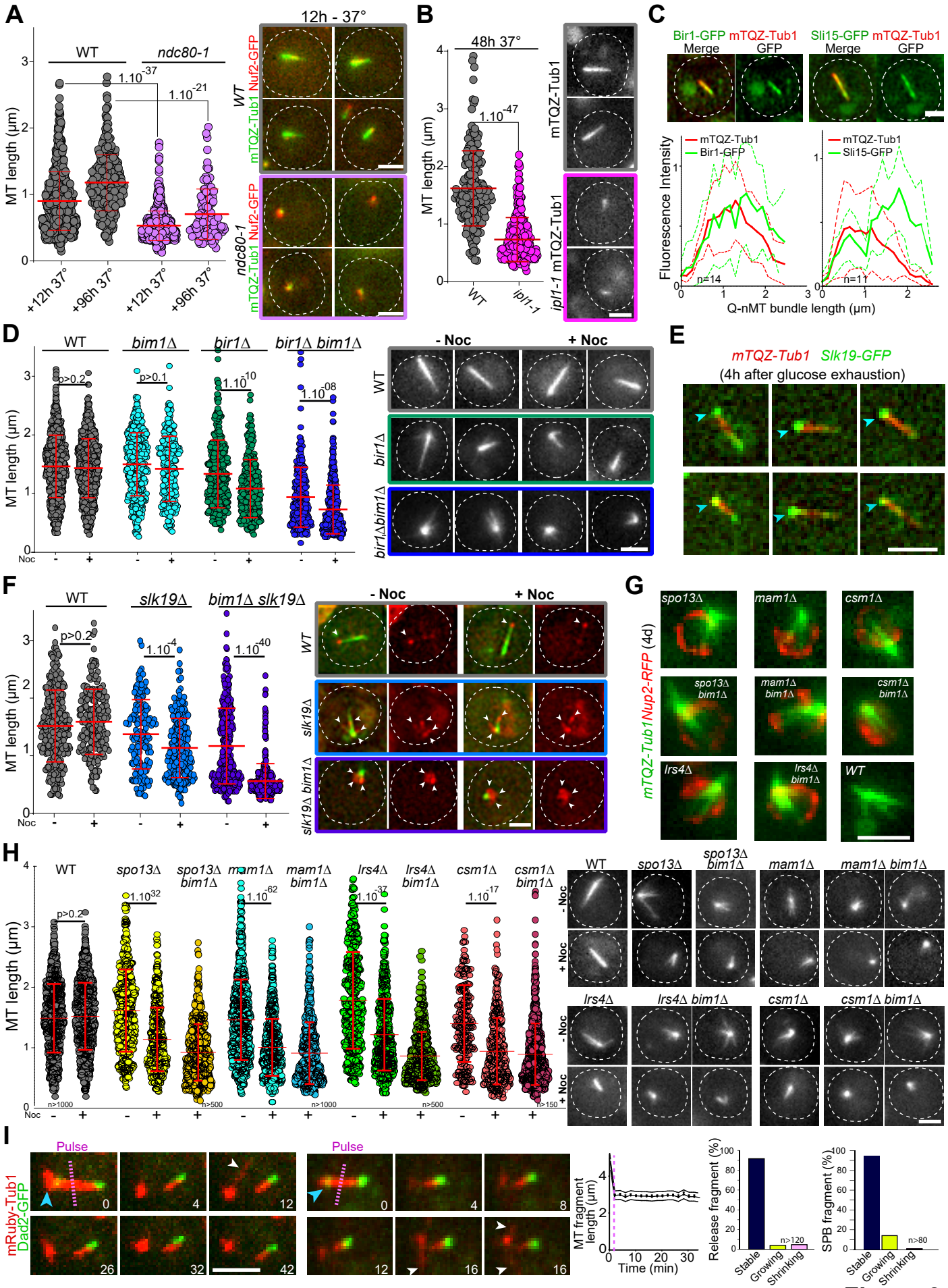
A
12h - 37°
WT
ndc80-1
MT length (µm)
+12h 37°
+96h 37°
mTQZ-Tub1 Nuf2-GFP
B
48h 37°
mTQZ-Tub1
ipl1-1
C
Bir1-GFP mTQZ-Tub1
Sli15-GFP mTQZ-Tub1
Merge
GFP
Fluorescence Intensity
Q-nMT bundle length (µm)
D
bim1Δ
bir1Δ
bir1Δ bim1Δ
- Noc
+ Noc
E
mTQZ-Tub1 Slk19-GFP
(4h after glucose exhaustion)
F
slk19Δ
bim1Δ slk19Δ
G
spo13Δ
mam1Δ
csm1Δ
lrs4Δ
mTQZ-Tub1Nup2-RFP (4d)
H
spo13Δ bim1Δ
mam1Δ bim1Δ
lrs4Δ bim1Δ
csm1Δ bim1Δ
I
Pulse
mRuby-Tub1
Dad2-GFP
MT fragment length (µm)
Time (min)
Release fragment (%)
SPB fragment (%)
Stable
Growing
Shrinking

Figure 3

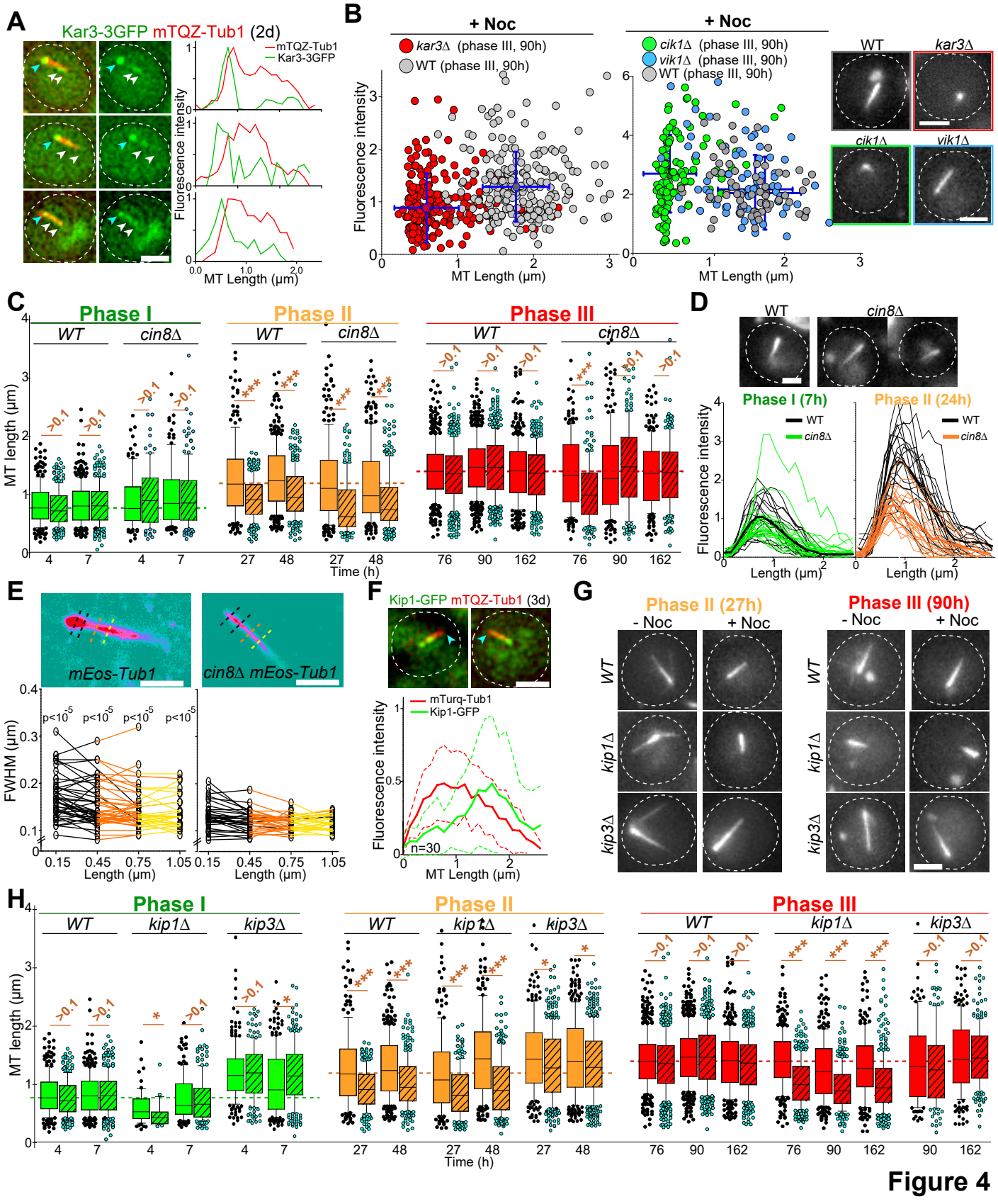
A
Kar3-3GFP mTQZ-Tub1 (2d)
mTQZ-Tub1
Kar3-3GFP
Fluorescence intensity
MT Length (µm)
B
+ Noc
kar3Δ (phase III, 90h)
WT (phase III, 90h)
Fluorescence intensity
MT Length (µm)
+ Noc
cik1Δ (phase III, 90h)
vik1Δ (phase III, 90h)
WT (phase III, 90h)
MT Length (µm)
WT
kar3Δ
cik1Δ
vik1Δ
C
Phase I
Phase II
Phase III
WT
cin8Δ
MT length (µm)
Time (h)
D
WT
cin8Δ
Phase I (7h)
Phase II (24h)
Fluorescence intensity
Length (µm)
E
mEos-Tub1
cin8Δ mEos-Tub1
FWHM (µm)
Length (µm)
F
Kip1-GFP mTQZ-Tub1 (3d)
mTurq-Tub1
Kip1-GFP
Fluorescence intensity
n=30
MT Length (µm)
G
Phase II (27h)
Phase III (90h)
- Noc
+ Noc
WT
kip1Δ
kip3Δ
H
Phase I
Phase II
Phase III
WT
kip1Δ
kip3Δ
MT length (µm)
Time (h)

Figure 4

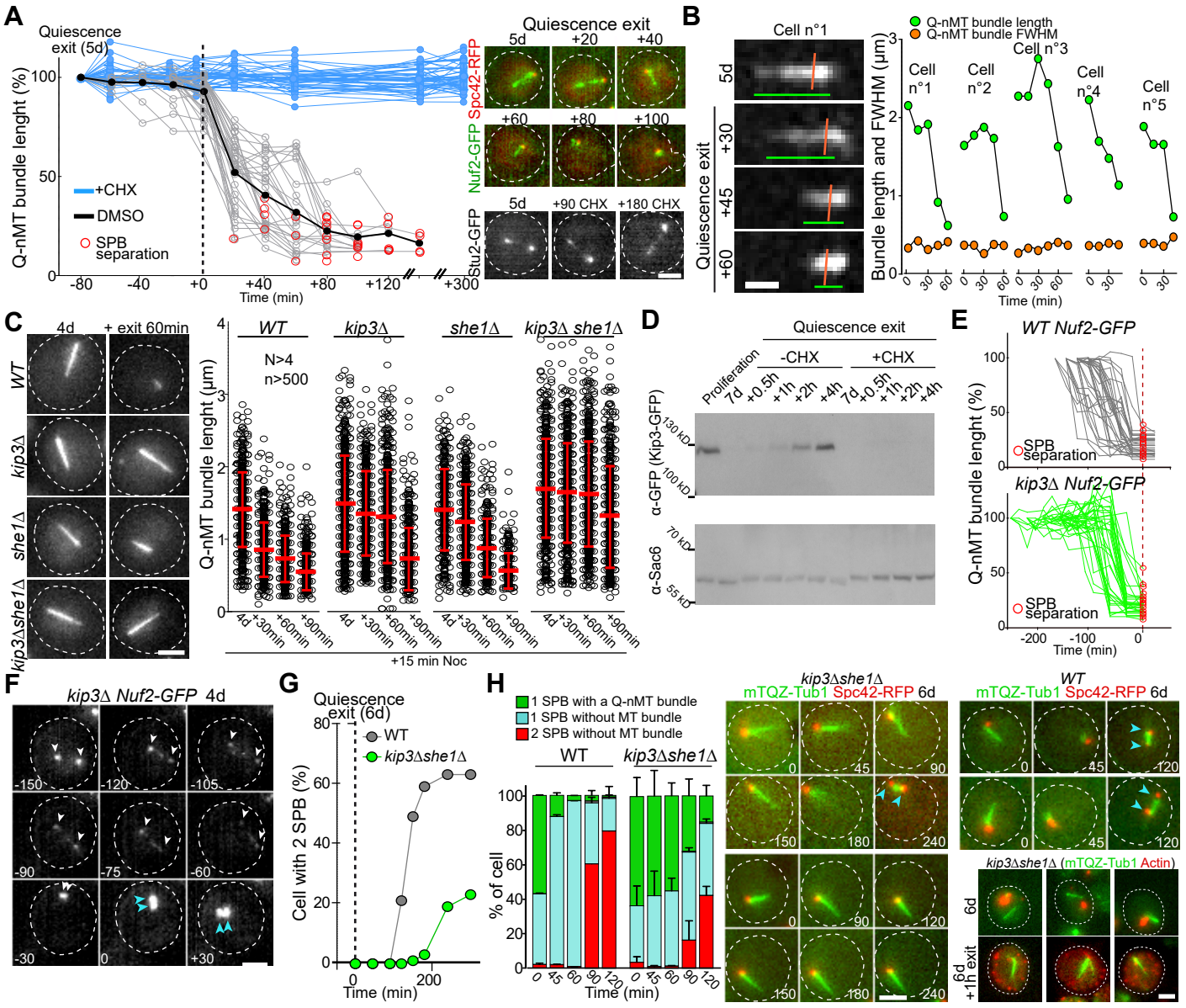
A
Quiescence exit (5d)
Q-nMT bundle lenght (%)
+CHX
DMSO
SPB separation
Time (min)
Quiescence exit
5d
+20
+40
+60
+80
+100
Spc42-RFP
Nuf2-GFP
Stu2-GFP
+90 CHX
+180 CHX
B
Cell n°1
Cell n°2
Cell n°3
Cell n°4
Cell n°5
Q-nMT bundle length
Q-nMT bundle FWHM
Bundle length and FWHM (µm)
Quiescence exit
+30
+45
+60
C
4d
+ exit 60min
WT
kip3Δ
she1Δ
kip3Δshe1Δ
N>4
n>500
Q-nMT bundle lenght (µm)
+15 min Noc
D
Quiescence exit
Proliferation
-CHX
+CHX
α-GFP (Kip3-GFP)
α-Sac6
130 kD
100 kD
70 kD
55 kD
E
WT Nuf2-GFP
kip3Δ Nuf2-GFP
Q-nMT bundle lenght (%)
SPB separation
Time (min)
F
kip3Δ Nuf2-GFP 4d
G
Quiescence exit (6d)
WT
kip3Δshe1Δ
Cell with 2 SPB (%)
Time (min)
H
1 SPB with a Q-nMT bundle
1 SPB without MT bundle
2 SPB without MT bundle
% of cell
kip3Δshe1Δ
mTQZ-Tub1 Spc42-RFP 6d
WT
mTQZ-Tub1 Spc42-RFP 6d
kip3Δshe1Δ (mTQZ-Tub1 Actin)
6d
6d +1h exit

Figure 5

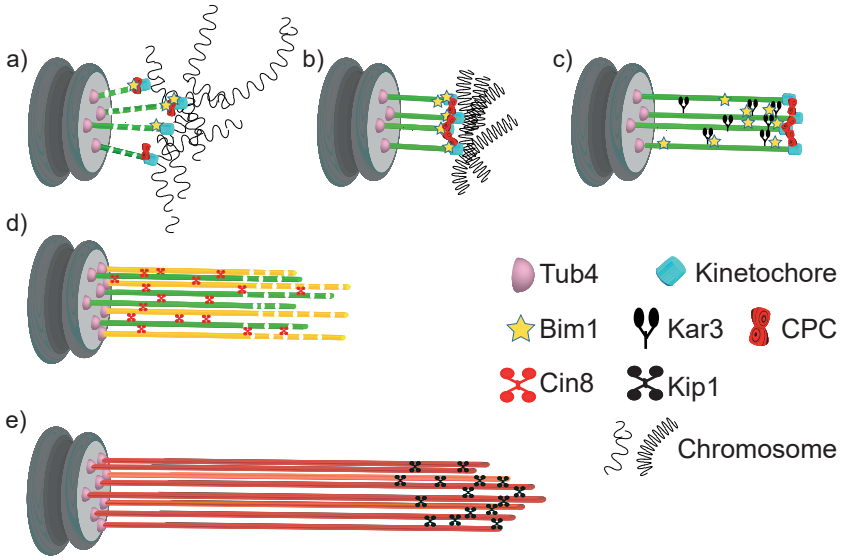

Figure 6